

WFOT: A Wave Function Overlap Tool between Single- and Multi-Reference Electronic Structure Methods for Spectroscopy Simulation

Alessandro Loreti, Victor Manuel Freixas, Davide Avagliano, Francesco Segatta, Huajing Song, Sergei Tretiak, Shaul Mukamel, Marco Garavelli,* Niranjana Govind,* and Artur Nenov*



Cite This: *J. Chem. Theory Comput.* 2024, 20, 4804–4819



Read Online

ACCESS |



Metrics & More

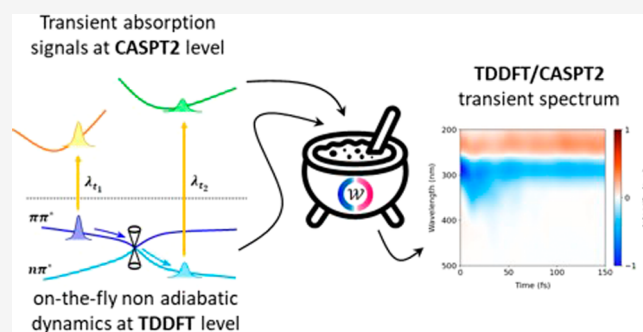


Article Recommendations



Supporting Information

ABSTRACT: We report the development of a novel diagnostic tool, named wave function overlap tool (WFOT), designed to evaluate the overlap between wave functions computed at single-reference [i.e., time-dependent density functional theory or configuration interaction singles (CIS)] and multireference (i.e., CASSCF/CASPT2) electronic structure levels of theory. It relies on truncating the single- and multireference WFs to CIS-like expansions spanning the same configurational space and maximizing the molecular orbital overlap by means of a unitary transformation. To demonstrate the functionality of the tool, we calculate the transient spectrum of acetylacetone by evaluating excited state absorption signals with multireference quality on top of single-reference on-the-fly dynamics simulations. Semiautomatic spectra generation is facilitated by interfacing the tool with the COBRAMM package, which also allows one to use WFOT with several quantum chemistry codes such as Gaussian, NWChem, and OpenMolcas. Other exciting possibilities for the utilization of the code beyond the simulation of transient absorption spectroscopy are eventually discussed.



1. INTRODUCTION

In the field of excited state electronic structure calculations, the class of single-reference (SR) methods offers an immense computational speed up in comparison to multireference (MR) methods, often with accuracy comparable to the latter. Linear response time-dependent density functional theory (LR-TDDFT)^{1,2} is arguably the most widespread member of this class. For example, LR-TDDFT is nowadays routinely employed for simulating nonadiabatic photoinduced dynamics in the manifold of valence excited states for systems having tens of heavy atoms in combination with trajectory-based mixed quantum-classical dynamics methods such as Tully's fewest switches surface hopping (FSSH).^{3–6} Other SR techniques include, but are not limited to, the configuration interaction singles (CIS), the time-dependent Hartree–Fock theory, and the LR-Tamm–Dancoff approximation (LR-TDA-DFT) to LR-TDDFT.

The SR methods such as LR-TDDFT have one conceptual limitation, namely, electronic states with substantial multiple excitation character (beyond single excitations) cannot be treated within the linear response formalism. This includes the case when the usual adiabatic approximation is applied for the exchange–correlation kernel.^{7,8} Furthermore, due to the Brillouin Theorem,⁹ the potential energy surfaces (PESs) near conical intersections (CoIn) between the ground state (GS or

S_0) and the first excited state (S_1) cannot be described with the SR methods as well.¹⁰ States of multiple excitation character formed from the GS Slater determinant usually have high energies, making them unacceptable for modeling of UV/vis photoinduced dynamics^a. Yet, their accurate description is indispensable for simulating transient absorption spectroscopy (TAS) where doubly excited states give rise to state-specific photoinduced absorption (PA) features that are used to measure the time scales of the photoinduced processes. The development of schemes for incorporating double excitations in the TDDFT formalism is an active field of research. For example, dressed TDDFT^{12–15} has been proposed as a posteriori correction to the adiabatic approximation of the exchange–correlation kernel.

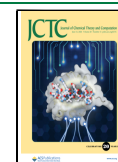
Other approaches such as multireference spin-flip TDDFT¹⁶ and constrained variational methods,¹⁷ such as Δ SCF,¹⁸ and the maximum overlap method^{19–21} rely on an open-shell Slater determinant as a reference from which desired doubly excited

Received: March 9, 2024

Revised: May 9, 2024

Accepted: May 15, 2024

Published: June 3, 2024



states can be created by promoting single electrons. Here, doubly excited states can be brought within the operational range of the LR formalism.²² Neither of the above methods has been yet extensively benchmarked to assess their performance and generality. Thus, despite ongoing efforts,^{23–26} a robust and universally applicable approach for incorporating double excitations in the TDDFT formalism is still largely missing.

In contrast, electronic configurations characterized by multiple excitations are an integral part of the wave function definition of multireference methods, which allow treating singly and multiply excited electronic states on an equal footing. The complete active space self-consistent field (CASSCF) method corrected by second-order perturbation theory (CASPT2)—the CASSCF/CASPT2 protocol and its restricted active space variation RASSCF/RASPT2, scaling more favorably with the active space size, are among the most popular methods within the multireference class. These techniques combine the variational treatment of a subset of electrons and orbitals—the *active space*—with a perturbative treatment of the remaining bulk. The completeness of PT2-simulated TAS and their remarkable agreement with experiments have been demonstrated on several occasions.^{27–30} However, the unfavorable exponential scaling of the CASSCF/CASPT2 and RASSCF/RASPT2 protocols remains detrimental for problems involving dynamics, limiting their practical application to systems of about ten heavy atoms and simulations on the sub-ps time scale. In fact, the list of reported PT2 on-the-fly dynamics simulations is rather limited. This may be particularly attributed to the absence of numerically accessible analytical gradients critical for dynamical simulations, which have become available only recently.^{28,31–40}

Therefore, it is advantageous to leverage the strengths of both single- and multireference classes of theories: the computational efficiency of dynamics simulations provided by single-reference methods and the completeness of the electronic structure spectrum offered by multireference methods. Achieving this synergy is not trivial. Even in selected cases where single- and multireference methods provide comparable descriptions of the electronic structure within the valence manifold, variations in the treatment of (dynamic) correlation result in crossings between adiabatic potential energy surfaces appearing at distinct regions of the nuclear coordinate space. This leads to a mismatch in the state ordering and inconsistencies in state-mixing along the dynamics. Reordering the states by only comparing the CI coefficients of the single- and multireference wave functions is not only extremely time-consuming but also potentially detrimental: the two methods rely on different molecular orbitals (MOs) with distinct spatial extent and energy ordering. The problem of state mismatch could potentially be addressed with an automatic tool for mapping the manifolds of the single- and multireference calculations onto each other.

In this contribution, we present a practical tool for accomplishing the goal of using side-by-side single- and multireference methods, a code for computing the overlap between LR-TDDFT (within LR-TDA-DFT) and CASPT2 wave functions by truncating them to CIS-like expansions spanning the same configurational space in the postprocessing, as will be elaborated below. The code allows for the automatic mapping onto each other of the manifold of TDDFT states provided by QM codes such as NWChem^{41–43} and Gaussian,⁴⁴ and the manifold of PT2 states computed with QM codes such as OpenMolcas.^{45,46} The integration of the code in the COBRAMM package for on-the-fly dynamics and spectroscopy simulations facilitates the automatized simulation of transient

absorption and photoemission spectra with CASPT2 accuracy on top of LR-TDA-DFT on-the-fly dynamics. This makes possible a straightforward generalization to other quantum chemistry codes and methods.

We showcase the utility of the code using the $S_2 \rightarrow S_1$ internal conversion (IC) in acetylacetone (AcAc)^{47–51} as an illustrative example. Specifically, a swarm of independent of-the-fly trajectories run with Tully's FSSH algorithm at the LR-TDA-DFT level successfully captures the ultrafast nature of the process. Subsequently, the electronic structure of the valence manifold is computed up to the ionization limit (ca. 9 eV) at the CASPT2 level. The wave function overlap (WFO) code is then used to identify the CASPT2 states on which the LR-TDA-DFT photoactive state, i.e., the state in which the dynamics reside at each time step, projects. Finally, the COBRAMM suite is utilized to compute the PA features of the photoactive state and to assemble the TAS.

AcAc has been selected to demonstrate the implementation for two reasons.

- a the nature of the two lowest-lying electronic states, a bright $\pi\pi^*$ and a dark $n\pi^*$, allows for an alternative mapping approach of the LR-TDA-DFT and CASPT2 manifold onto each other, namely, by analyzing the transition dipole moments (TDM) magnitudes. This facilitates an independent way to assess the correctness of the WFO implementation;
- b The TA fingerprints of the $\pi\pi^*$ and $n\pi^*$ states are of predominantly doubly excited nature with configurations π^{*2} and $n\pi\pi^{*2}$, respectively. This makes them inaccessible within the LR-TDA-DFT framework while being accurately captured at the CASPT2 level.

The paper is structured as follows. In the **Methods** section, we outline the procedure for computing the overlap between single- and multireference WF (generalized to different basis sets) and the functionality of the code as an independent unit and as a part of COBRAMM. In the **Results** section, we first show illustrative examples of the LR-TDA-DFT to CASPT2 mapping based on AcAc on-the-fly trajectories. Next, we document the complete TAS for the $S_2 \rightarrow S_1$ IC process. Finally, in the **Conclusion**, we discuss exciting possibilities for adapting the code to applications beyond the simulation of TAS.

2. METHODS

One of the most interesting applications of the presented tool is to simulate transient spectroscopy with multireference methods such as CASPT2 on top of on-the-fly nonadiabatic mixed quantum-classical trajectories simulated at a single-reference level of theory such as LR-TDDFT. This relies on the key assumption that the single-reference method correctly describes the photophysics of the system. The multireference method is used to obtain a complete description of the manifold of higher-lying states such as doubly excited states. In the following, we first outline the protocol for computing the WFO between LR-TDDFT wave functions (or pseudowave functions) calculated within the Tamm–Dancoff approximation and PT2 wave functions, needed in order to map the TDDFT photoactive state onto the PT2 manifold. Next, we derive the equations for the previously defined PA and stimulated emission (SE) contributions to the transient spectrum. Finally, we detail the interface of the tool with the COBRAMM suite for hybrid QM/MM dynamics and spectroscopy simulations, which makes use

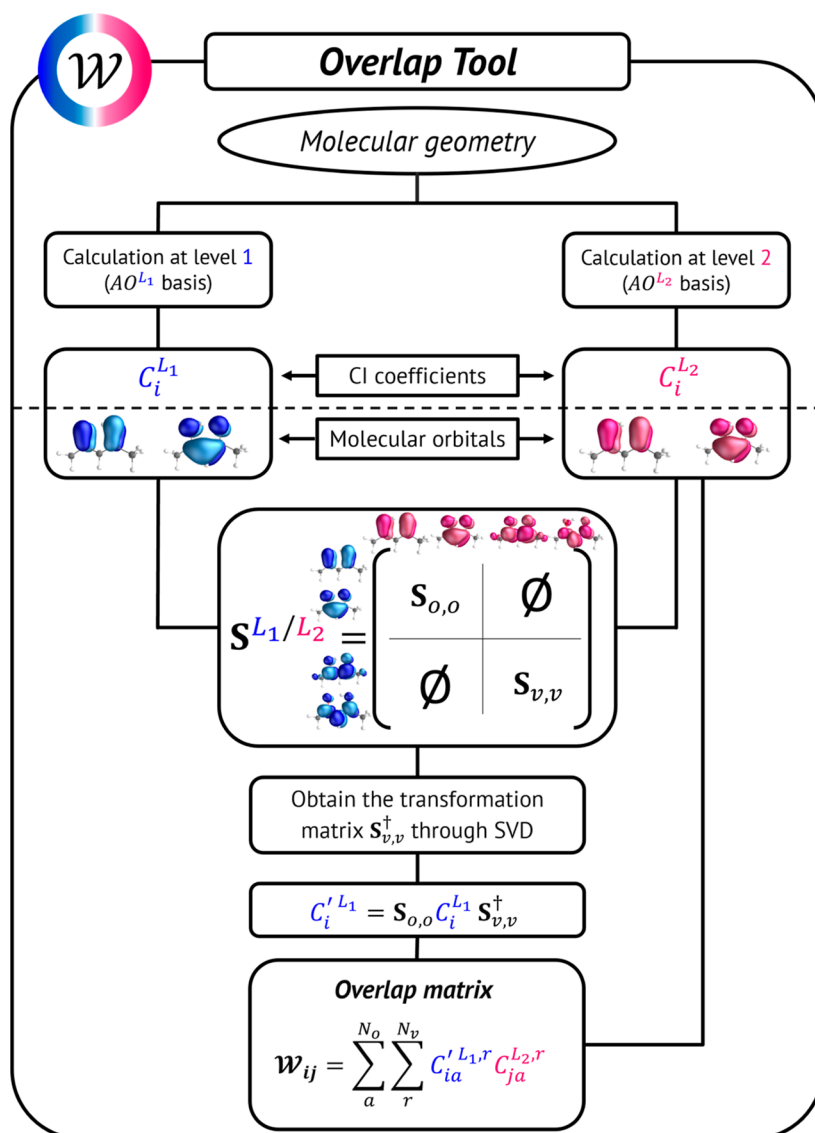


Figure 1. Summarized workflow of the WFO tool, applied on a single geometry. Calculation levels L_1 and L_2 refer to TDDFT and CASPT2, respectively. Here, the more general protocol is presented which facilitates WFOs between single- and multireference electronic structure methods performed with different basis sets.

b In the vicinity of the seam, the S_0 and S_1 states are usually energetically well separated from the higher lying excited states (a notable exception here is three state CoIns⁶¹) so that mapping of the active TDDFT state onto the PT2 manifold is straightforward.

Under the assumption of nonmixing occupied and virtual MOs, the overlap matrix $\mathbf{S}^{\text{DFT/CAS}}$ becomes block-diagonal

$$\mathbf{S}^{\text{DFT/CAS}} = \begin{pmatrix} \mathbf{S}_{o,o} & 0 \\ 0 & \mathbf{S}_{v,v} \end{pmatrix} \quad (6)$$

Moreover, the assumption implies that each subset of MOs (occupied and virtual) is complete^b. Therefore, there exist unitary transformation matrices \mathbf{U}_o and \mathbf{U}_v that maximize the overlap between occupied–occupied and virtual–virtual orbitals obtained from DFT and CAS methods. Since, in practice, the off-diagonal blocks $\mathbf{S}_{o,v}$ and $\mathbf{S}_{v,o}$ are not zero, the transformation matrices are obtained through Löwdin orthonormalization

$$\frac{\mathbf{S}_{o,o}^T (\mathbf{S}_{o,o} \mathbf{S}_{o,o}^T)^{-1/2}}{\mathbf{U}_o} \mathbf{S}_{o,o} = \mathbf{I} \quad \text{and} \quad \frac{\mathbf{S}_{v,v}^T (\mathbf{S}_{v,v} \mathbf{S}_{v,v}^T)^{-1/2}}{\mathbf{U}_v} \mathbf{S}_{v,v} = \mathbf{I} \quad (7)$$

With the above MO transformations, the MO overlap matrix becomes a unit matrix. Consequently, in this rotated orbital basis, only elements of the determinant overlap terms $\langle \Phi_a^{\text{TDDFT},r} | \Phi_b^{\text{PT2},s} \rangle$ with identical *bra* and *ket* terms survive, i.e.

$$\langle \Phi_a^{\text{TDDFT},r} | \Phi_b^{\text{PT2},s} \rangle = \delta_{ab} \delta_{rs} \quad (8)$$

which simplifies the calculation of the WFO to a sum of products of CI coefficients

$$\mathcal{W}_{ij}^{\text{TDDFT/PT2}} = \sum_a^{N_o} \sum_r^{N_v} C_{ia}'^{\text{TDDFT},r} C_{ja}^{\text{PT2},r} \quad (9)$$

The $C_{ia}'^{\text{TDDFT},r}$ coefficients are obtained by applying the transformation matrices \mathbf{U}_o and \mathbf{U}_v to the set of LR-TDDFT

CI coefficients of the i -th ES, organized in a rectangular matrix $\mathbf{C}_i^{\text{TDDFT}}$ with the a, r -th element corresponding to the coefficient of the determinant generated from the closed shell determinant by exciting an electron from a to r MOs, so that

$$\mathbf{C}_i^{\text{TDDFT}} = \mathbf{U}_o^T \mathbf{C}_i^{\text{TDDFT}} \mathbf{U}_v \quad (10)$$

In passing, we note that the alternative transformation of the PT2 CI-coefficients is equally viable to obtain the WFO.

To this end, we assume that both levels of theory employ the same basis set, implying that the MO overlap matrix \mathbf{S} is square. We now extend the protocol to the more general case of different basis sets with distinct lengths m and n used for the single- and multireference calculations, respectively. It is obvious that the occupied–occupied block $\mathbf{S}_{o,o}$ has the same size (i.e., $N/2 \times N/2$). However, the virtual–virtual block $\mathbf{S}_{v,v}$ will have a rectangular shape ($o \times p$, with $o = m - N/2$ and $p = n - N/2$) due to the excess of virtual MOs in the case of the larger basis set. The transformation matrix of $\mathbf{S}_{v,v}$ that maximizes the overlap between the two sets of MOs can be obtained through singular value decomposition (SVD), which allows to write a rectangular matrix as a product of three matrices

$$\mathbf{S}_{v,v} = \mathbf{U} \times \mathbf{D} \times \mathbf{V}^T \quad (11)$$

where \mathbf{U} and \mathbf{V} are symmetric matrices with $o \times o$ and $p \times p$ shapes, respectively, while \mathbf{D} is a $o \times p$ rectangular matrix with nonzero diagonal elements, called eigenvalues. The SVD allows us to formulate the pseudoinverse

$$\mathbf{S}_{v,v}^\dagger = \mathbf{V} \times \mathbf{D}^{-1} \times \mathbf{U}^T \quad (12)$$

with $p \times o$ shape. The matrix \mathbf{D}^{-1} , with dimensions $p \times o$, is derived by computing the reciprocal of the nonzero diagonal elements of \mathbf{D} . The incompleteness of the v, v block requires rounding off the eigenvalues of \mathbf{D} prior to inverting it to 1 or 0 to ensure normalization.

Equipped with the pseudoinverse matrix, we are now in a position to generalize eq 10

$$\mathbf{C}_i^{\text{TDDFT}} = \mathbf{S}_{o,o} \mathbf{C}_i^{\text{TDDFT}} \mathbf{S}_{v,v}^\dagger \quad (13)$$

Note that upon the transformation the matrix of CI-coefficients of the i -th electronic state, $\mathbf{C}_i^{\text{TDDFT}}$ is reshaped from $N/2 \times p$ to $N/2 \times o$. If $p < o$, this essentially means that determinants generated via transitions to the excess virtual orbitals in the larger basis set are removed, leaving only those determinants generated by transitions among the common subset of MOs. Employing the pseudoinverse matrix enables the treating of even unorthodox scenarios in which the two basis sets span different variable spaces, e.g., double- ζ with polarizable vs diffuse functions. This can result in (near-)zero-valued rows/columns in the $\mathbf{S}_{v,v}$ block of the MO overlap matrix with (near-)zero eigenvalues. The workflow of the WFO tool is visually summarized in Figure 1.

2.2. Transition Energies and Dipole Moments. After completing the mapping of TDDFT and PT2 states' manifolds using the method described above, we can apply it for computing transient absorption spectroscopy. Here, we derive expressions for the transition energies and dipole moments from the photoactive state to the GS and to the manifold of higher-lying states, i.e., the ingredients necessary to compute the SE and TA contributions of each on-the-fly trajectory to the transient spectrum.

At any given geometry, one can define the projection operator over a complete set of PT2 WFs

$$\hat{\mathbf{I}} = \sum_j |\Psi_j^{\text{PT2}}\rangle \langle \Psi_j^{\text{PT2}}| \quad (14)$$

which applied to the i -th state from the TDDFT manifold $|\Psi_i^{\text{TDDFT}}\rangle$ allows to express it in the basis of the PT2 states

$$|\Psi_i^{\text{TDDFT}}\rangle = \sum_j |\Psi_j^{\text{PT2}}\rangle \langle \Psi_j^{\text{PT2}} | \Psi_i^{\text{TDDFT}}\rangle = \sum_j \mathcal{W}_{ij} |\Psi_j^{\text{PT2}}\rangle \quad (15)$$

Here, the coefficients \mathcal{W}_{ij} are precisely the elements of the WFO, where we removed the TDDFT|PT2 superscript to simplify the notation. In practice, the PT2 projector is constructed over the few lowest PT2 states, which are assumed to represent a nearly complete basis set to represent the i th photoactive TDDFT state's WF at any given geometry. Due to the truncation of the PT2 WF to singly excited determinants, they do not form a normalized basis. This requires normalizing the WFO matrix.

The PT2 expectation value of the energy of the i th TDDFT state's WF at a geometry $\mathbf{R}_n(T)$ visited by the n th on-the-fly trajectory at time T is expressed on the basis of the PT2 WFs

$$\begin{aligned} E_i^{\text{TDDFT}}(\mathbf{R}_n(T)) &= \langle \Psi_i^{\text{TDDFT}} | \hat{H} | \Psi_i^{\text{TDDFT}} \rangle_{\mathbf{R}_n(T)} \\ &= \sum_{j,k} \mathcal{W}_{ij}(\mathbf{R}_n(T)) \mathcal{W}_{ik}(\mathbf{R}_n(T)) \\ &\quad \delta_{jk} \langle \Psi_j^{\text{PT2}} | \hat{H} | \Psi_k^{\text{PT2}} \rangle_{\mathbf{R}_n(T)} \\ &= \sum_j \mathcal{W}_{ij}^2(\mathbf{R}_n(T)) E_j^{\text{PT2}}(\mathbf{R}_n(T)) \end{aligned} \quad (16)$$

where $|\Psi_k^{\text{PT2}}\rangle$ are eigenfunctions of the PT2 Hamiltonian at the geometry $\mathbf{R}_n(T)$. Thus, the PT2 energy of the i -th TDDFT state is simply a weighted sum of the energies of the PT2 states with weighting factors equal to the squared elements of the WFO matrix. Transition energies to the GS and to higher-lying states, obtained in a PT2 calculation usually with several tens of excited states, are computed with respect to the energy expectation value of the photoactive state.

The TDMs of the i th TDDFT WF expressed on the basis of the PT2 WFs read

$$\begin{aligned} \mu_{ij}^{\text{TDDFT} \rightarrow \text{PT2}}(\mathbf{R}_n(T)) &= \langle \Psi_i^{\text{TDDFT}} | \hat{\mu} | \Psi_j^{\text{PT2}} \rangle_{\mathbf{R}_n(T)} \\ &= \sum_k \mathcal{W}_{ik}(\mathbf{R}_n(T)) \\ &\quad \langle \Psi_k^{\text{PT2}} | \hat{\mu} | \Psi_j^{\text{PT2}} \rangle_{\mathbf{R}_n(T)} \\ &= \sum_k \mathcal{W}_{ik}(\mathbf{R}_n(T)) \\ &\quad \mu_{kj}^{\text{PT2} \rightarrow \text{PT2}}(\mathbf{R}_n(T)) \end{aligned} \quad (17)$$

The matrix elements of every other single particle operator can be similarly computed.

2.3. Implementation of the WFO Protocol in CO-BRAMM. Having obtained expressions for transition energies and dipole moments, we are in a position to simulate the TA spectrum. The TA signals at each delay time T between the pump and the probe pulse are given as a sum of three contributions over all trajectories

$$\begin{aligned}
 I(E, T) & \\
 \propto & - \sum_n \sum_e |\mu_{ge}|^2 \exp \left[- \frac{(\Delta E_{eg}(\mathbf{R}_n(T=0)) - E)^2}{2\sigma^2} \right] \\
 & - \sum_n |\mu_{a_n g}|^2 \exp \left[- \frac{(\Delta E_{a_n g}(\mathbf{R}_n(T)) - E)^2}{2\sigma^2} \right] \\
 & + \sum_n \sum_f |\mu_{a_n f}|^2 \exp \left[- \frac{(\Delta E_{fa_n}(\mathbf{R}_n(T)) - E)^2}{2\sigma^2} \right]
 \end{aligned}
 \tag{18}$$

where the index n runs over all trajectories, and the index a_n denotes the photoactive state in which the n -th trajectory resides at time T . e and f denote the manifolds of states under the probe envelope with respect to the GS (labeled g) and to the photoactive states, respectively. σ denotes the standard deviation, a phenomenological parameter used to broaden spectral contributions due to dephasing, environment-induced static disorder, and finite excited state lifetimes. The first term in eq 18, known as the ground state bleach, is a time-independent quantity. It represents the reduced absorption of the molecules in the ground state after the pump pulse has excited a portion of the population to excited states. The second and third terms represent the SE and excited state absorption (ESA), respectively. These terms vary with the pump–probe delay time and signify the emission and absorption processes occurring within the ensemble of trajectories evolving in the excited state manifold. Note that ESA contributions have opposite signs with respect to ground state bleaching (GSB) and SE.

For the practical realization, the WFO tool has been integrated into the suite COBRAMM⁶² and is made available in COBRAMM's GitLab repository (<https://gitlab.com/cobrammgroup/cobramm>). COBRAMM already disposes of the infrastructure for on-the-fly mixed-quantum classical dynamics (i.e., Tully FSSH) and TA spectroscopy simulations at TDDFT⁶⁰ and CASPT2⁴⁶ levels of theory through interfaces with Gaussian⁴⁴ and OpenMolcas.⁴⁶

Notably, COBRAMM comes with an interface with the MM software Amber,⁶³ which allows us to consider solvent effects and complex environments in the TA spectroscopy simulations at the QM/MM level with electrostatic embedding. Among other useful tools is the interface with the code iSpectron,⁶⁴ which provides a rich palette of spectra postprocessing tools (e.g., temporal convolution and Fourier transform of quantum beatings) and an in-house routine for computing atomic orbital (AO) overlap. This feature is essential for computing the MO overlap matrix $\mathbf{S}^{\text{DFTICAS}}$ required by the WFO analysis, especially when different basis sets are used for the single- and multireference calculations

$$\mathbf{S}^{\text{DFTICAS}} = \mathbf{c}^{\text{DFT}} \mathbf{S}^{\text{bs1bs2}} \mathbf{c}^{\text{CAS}}
 \tag{19}$$

where \mathbf{c}^{DFT} and \mathbf{c}^{CAS} are the matrices of MO coefficients of the two calculations and $\mathbf{S}^{\text{bs1bs2}}$ is the rectangular AO overlap matrix between the basis functions of the two basis sets bs1 and bs2. To this aim, the functionality of the COBRAMM in-house AO overlap tool has been extended to process a number of basis sets (e.g., Pople's, cc-pVXZ, ANO) through an interface with the Basis Set Exchange⁶⁵ database.

The WFO tool can function as a stand-alone feature for mapping WFs, currently interfaced with Gaussian, NWChem,⁴²

and OpenMolcas and limited to identical basis sets⁶. The modular structure of the code renders interfacing with other QM software straightforward. For the current work, we manually processed the output of Tully FSSH mixed quantum-classical dynamics performed with a development version of NWChem to compute the higher-lying ES at the CASPT2 level and to generate the TA spectra (Figure 2). A COBRAMM-NWChem interface is currently in the making.

2.4. Computational Details. 2.4.1. LR-TDA-DFT On-the-Fly Nonadiabatic Dynamics. On-the-fly mixed quantum-

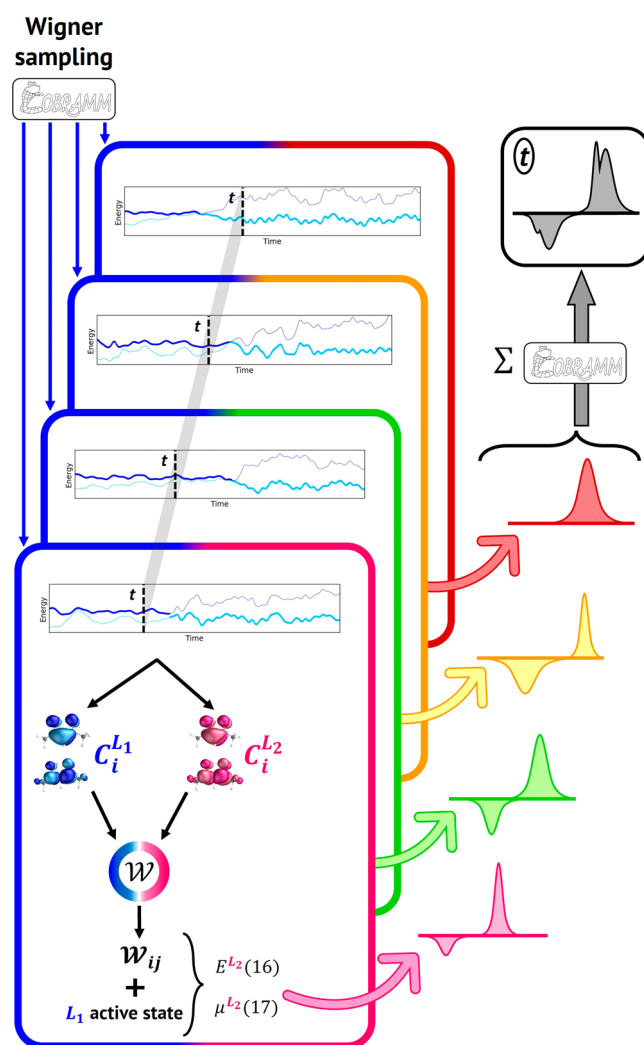


Figure 2. Workflow of transient absorption spectroscopy simulation on top of trajectory-based dynamics performed with COBRAMM utilizing single-to-multireference state mapping with the WFO tool. Calculation levels L_1 and L_2 refer to TDDFT and CASPT2, respectively. Wigner sampling provides initial conditions. Each trajectory is propagated at the TDDFT level (L_1). At selected geometries $\mathbf{R}(t)$ in defined time intervals, the electronic structure is recalculated at the CASPT2 level (L_2). The WFO tool maps the TDDFT manifold onto the CASPT2 one, thus obtaining the coefficients \mathcal{W}_{ij} , eqs 16 and 17 allow the computation of the CASPT2 expectation value of the energy of the i -th TDDFT state's WF and its transition dipole moments to other electronic states. Energetics and transition dipole moments are then used to compute the excited state absorption (ESA) and stimulated emission (SE) contributions to the transient signals from each trajectory at time t . The complete spectrum is obtained by spectral and temporal convolution provided by the COBRAMM utilities.

classical dynamics are run with NWChem via its internal Tully FSSH algorithm relying on time-derivative couplings (the so-called Tully–Hammes–Schiffer variation). WFO between consecutive time-steps (necessary for computing the time-derivative coupling numerically) is computed by means of the MO unitary transformation approach presented recently by some of the authors of this paper.⁶⁰ After the benchmark of several DFT functionals (namely, PBE0, M06, CAM-B3LYP, LC-wHPBE) in the Franck–Condon point against XMS-CASPT2 data (see Table 1 in the Supporting Information), the PBE0 functional is chosen for the dynamics complemented with cc-pVDZ basis set. This setup is used to propagate 45 independent trajectories for 250 fs with a time step of 0.5 fs. These trajectories are initiated in the spectroscopically accessible S_2 state with initial structures generated by Wigner sampling excluding a low-frequency methyl rotation and high-frequency C–H stretching modes. Four roots (excited states) are considered in these simulations.

2.4.2. CASSCF/CASPT2 Single Point Calculations. CASSCF calculations with a (10,8) active space, containing all π MOs and the two oxygen lone pair MOs, are performed at each timestep up to 150 fs averaging over 24 electronic states. Figures 1 and 2 in the Supporting Information show the shape of the MOs included in the active space. The energies and wave functions are corrected at the extended multistate (XMS) CASPT2 level of theory with imaginary shift and ionization potential electron affinity parameters set to 0.2 and 0.0 au, respectively. Including 24 states in the state averaging is required to capture the doubly excited states responsible for the ESA fingerprints of the S_1 and S_2 states. The XMS-CASPT2 wave functions are used to compute transition dipole moments. The basis set used is cc-pVDZ.

2.4.3. Spectra Simulation. The TA spectrum in the 225–500 nm (2.5–5.5 eV) range is obtained by summing over the SE and ESA contributions (eq 18) of all 45 trajectories. The GSB is added as a constant contribution due to the S_2 absorption at time zero. Convolution in the energy and time domains is performed with broadening values of 0.2 eV and 3 fs, respectively.

3. RESULTS

In the gas phase, the keto–enol equilibrium of acetylacetone is almost entirely shifted toward the enol form.⁶⁶ Upon photoexcitation with UV light, two singlet excited states are involved in the ultrafast IC: the spectroscopically dark $n\pi^*$ S_1 state and the bright $\pi\pi^*$ S_2 state. At the ground state optimal geometry, both XMS-CASPT2 and TDDFT agree on the energy of the dark $n\pi^*$ state (ca. 4.3 eV), but they disagree on the energetics of the $\pi\pi^*$ state (Table 1). With respect to the experimental value, TDDFT strongly overestimates its energy by ca. 1 eV across the entire set of four functionals explored in our benchmark, whereas XMS-CASPT2 underestimates it by ca. 0.2 eV (Table 1 in the Supporting Information). As it shall be demonstrated later, the immediate consequence of this discrepancy is that the CASPT2 energy profiles of the S_1 and S_2 adiabatic states show multiple crossings, not observed at the TDDFT level, which would significantly complicate a manual tracking of the state's character.

At the equilibrium geometries of the GS and $n\pi^*$ state, acetylacetone is an asymmetric molecule, with a clear distinction between hydroxy and oxy groups. In the equilibrium of the $\pi\pi^*$ state, instead, the hydrogen is equidistant and shared between the two oxygens. As a consequence, upon photoexcitation to the $\pi\pi^*$ state, an in-plane motion of the hydrogen is immediately

Table 1. Transition Energies of the First Two Singles Excited State alongside Their Oscillator Strength^a

	$n \rightarrow \pi^*$		$\pi \rightarrow \pi^*$	
	E (eV)	f	E (eV)	f
experimental	—	—	4.72 ⁶⁷	0.24 ⁶⁷
TDDFT	4.39	0.00	5.56	0.41
CASPT2	4.22	0.00	4.52	0.35
	$n\pi \Rightarrow \pi^*$		$\pi \Rightarrow \pi^*$	
CASPT2	9.53 (5.31)	0.00 (0.44)	9.69 (5.17)	0.00 (0.32)

^aExperimental values are reported where available alongside computed ones at the PBE0/TDDFT and XMS-24-CASPT2(10,8) level of theory. Additionally, the energies of the doubly excited bright states involved (computed at CASPT2 level) in the ESA are shown. Transition energies and oscillator strengths given in brackets are with respect to the corresponding singly excited state. Single and double arrows indicate single and double excitations (with respect to the ground state), respectively.

activated. Over the course of this motion, the $\pi\pi^*$ and $n\pi^*$ states cross leading eventually to the population of the lower lying $n\pi^*$ state. This, in turn, triggers the reformation of the hydroxy group, forcing the hydrogen to draw near one of the two oxygens (Figure 3). On a time scale of few picoseconds—out of the scope of the current work—the $n\pi^*$ state is deactivated by two competing mechanisms: a decay to the GS through a CI in which the structure is distorted from planarity and intersystem crossing to the triplet manifold.

3.1. LR-TDA-DFT On-the-Fly Dynamics. We start by discussing the TDDFT dynamics. Figure 4 shows the evolution of the electronic populations for the ensemble of trajectories, which shows a gradual depopulation in S_2 state on a sub-100 fs time scale accompanied by the concomitant buildup of the S_1 population (omitted in Figure 4). A monoexponential fit gives a time constant of 35 fs with an 8 fs offset (the decay onset), thus resulting in an effective $\pi\pi^*$ lifetime of ca. 45 fs. Figure 4 also tracks the brightness of the “active” state—the state in which the classical trajectory resides at each time step—averaged over the ensemble.

The two data sets are characterized by virtually identical decay profiles, with the S_2 occupation showing a minor delay, thus strongly suggesting that the change of nature of the active state occurs simultaneously with the $S_2 \rightarrow S_1$ hopping events. To deepen the analysis, in Figure 5, we show density plots of several structural degrees of freedom (internal coordinates) that best describe the dynamics of the system,⁶⁸ specifically two dihedral angles $\angle O_1C_2C_3C_4$ and $\angle C_2C_3C_4O_5$ that describe out-of-plane deformations of the conjugated chain (SA,B), the hydrogen transfer coordinate defined as $R_{O_1H} - R_{O_3H}$ (5C) and the bond length alternation coordinate defined as $0.5(R_{C_3C_4} + R_{C_2O_1} - R_{C_2C_3} - R_{C_3O_5})$.

Acetylacetone is planar in its GS equilibrium (Figure 5A,B). As the Wigner sampling is performed around one of the two identical GS minima in which the hydrogen is bound to O_1 , the hydrogen transfer coordinate has an initial value of ca. -0.5 Å, indicating the asymmetry in the hydrogen bonding (Figure 5C). Upon excitation, the gradient on the $\pi\pi^*$ state drives the hydrogen toward oxygen O_2 . This gives rise to a periodic back-and-forth motion with a 40 fs period, in phase with the bond length alternation oscillations in the conjugated chain (Figure 5D). During the second oscillation, around 45 fs and, thus, with almost all trajectories having decayed to S_1 , we observe

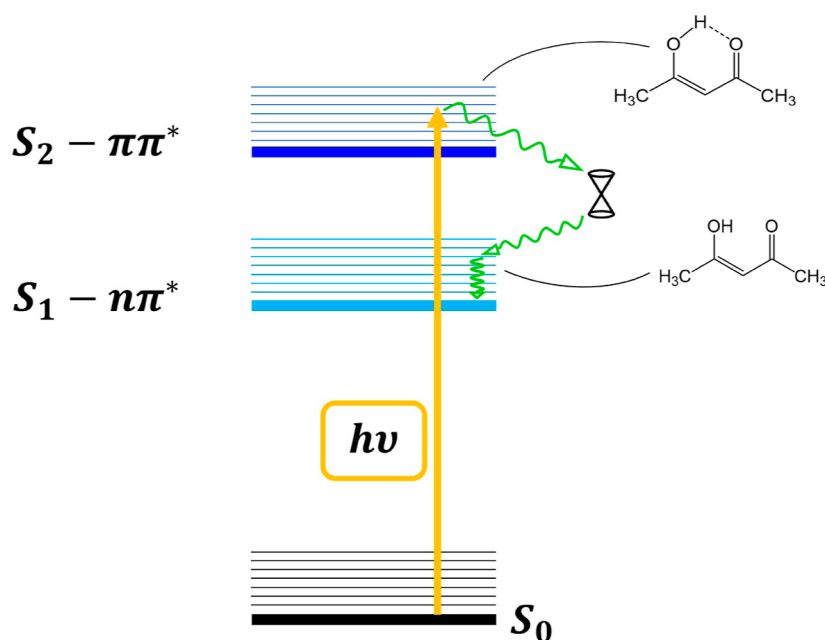


Figure 3. Energetic diagram of the deactivation pathway through the $\pi\pi^* \rightarrow n\pi^*$ CI seam.

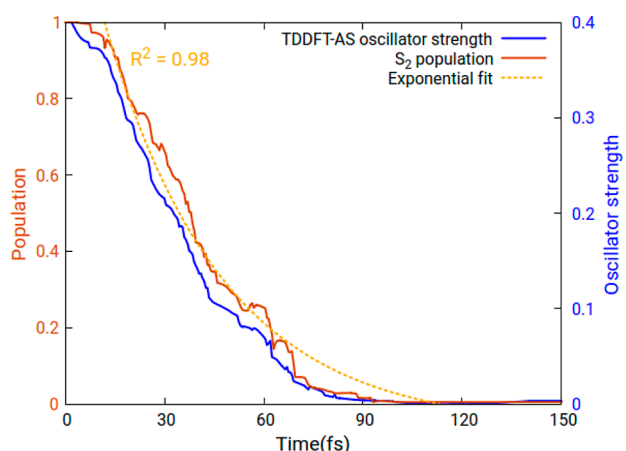


Figure 4. Occupation of the TDDFT S_2 state (brown) and oscillator strength of the active state (blue) over 150 fs, averaged over 45 trajectories. The orange dotted line represents a monoexponential curve fitting the S_2 occupation data from 8 fs onward.

trajectory splitting with the majority returning to the original configuration and a minor fraction exhibiting configuration inversion. Notably, the hydrogen transfer parameter acquires values of ± 1.5 , much larger than the initial value, which indicates its increased mobility (e.g., out-of-plane deformations). No further configuration inversion is observed during the evolution on S_1 despite the system continuing to exhibit bond length alternation dynamics (Figure 5D). The dihedral plots demonstrate that the backbone remains planar in the first few hundred fs (Figure 5A,B). As the dynamics progress, some kinetic energy is deposited into weak out-of-plane deformations (within the $\pm 30^\circ$) but the molecule never acquires pronounced torsional motion.

Next, we examine closer the energetic profiles along two representative trajectories. Figure 6B shows a straightforward case (sample 1), where the trajectory, initiated in S_2 , hops to S_1 after around 60 fs. Notably, the S_2 and S_1 states approach energetically already after 15 fs and, subsequently, every 20 fs.

Throughout the entire duration of the simulation, the S_2 and S_1 states can be unequivocally associated with the bright $\pi\pi^*$ state and dark $n\pi^*$ states, respectively, as evident from the oscillator strengths (Figure 6A). The change of the active state's nature coincides with the hopping event.

Figure 7B shows a somewhat less straightforward situation (sample 2). Energy-wise, the trajectory exhibits a similar behavior to sample 1, with the S_2 approaching the S_1 after 60 fs and eventually hopping after 80 fs. Examining the oscillator strengths (Figure 7A), one notices a nature change of the active state (from bright to dark) 5 fs preceding the hop. This is directly correlated to the slightly faster oscillator strength decay shown in Figure 4.

3.2. CASPT2 and WFO Calculations. The sample trajectories 1 and 2 examined in the previous paragraph are used here to demonstrate how the WFO tool facilitates mapping the CASPT2 onto the TDDFT electronic state manifolds.

Figure 6C reports the XMS-CASPT2 energy profiles of S_1 and S_2 states along the sample trajectory 1. Unlike the TDDFT profiles, the CASPT2 energy plot shows multiple crossings between the two adiabatic states due to a considerably smaller $S_1(n\pi^*)/S_2(\pi\pi^*)$ energy gap in the FC region. The crossings are accompanied by inversion of the character of the adiabatic states as confirmed by the CASPT2 oscillator strength profile (Figure 6D). Figure 6E shows the outcome of the WFO analysis. The essential information that can be extracted from this plot is to what extent the active TDDFT state maps onto the two CASPT2 states at each time step. It is clear that the active TDDFT state rarely maps entirely on a single CASPT2 state (that would correspond to a WFO value of 1). In the case of degeneracy at the CASPT2 level, the TDDFT state projects almost equally on both CASPT2 states. To improve data visualization, the outcome of the WFO analysis has been integrated within the CASPT2 energy (Figure 6C) and oscillator strength (Figure 6D) plots. In both subfigures, the line thickness is proportional to the squared WFO value and therefore can be used as a visual aid for tracking the active state in the CASPT2 profiles. A certain resemblance can be noted between the energy profiles of the active state's TDDFT and CASPT2 energy

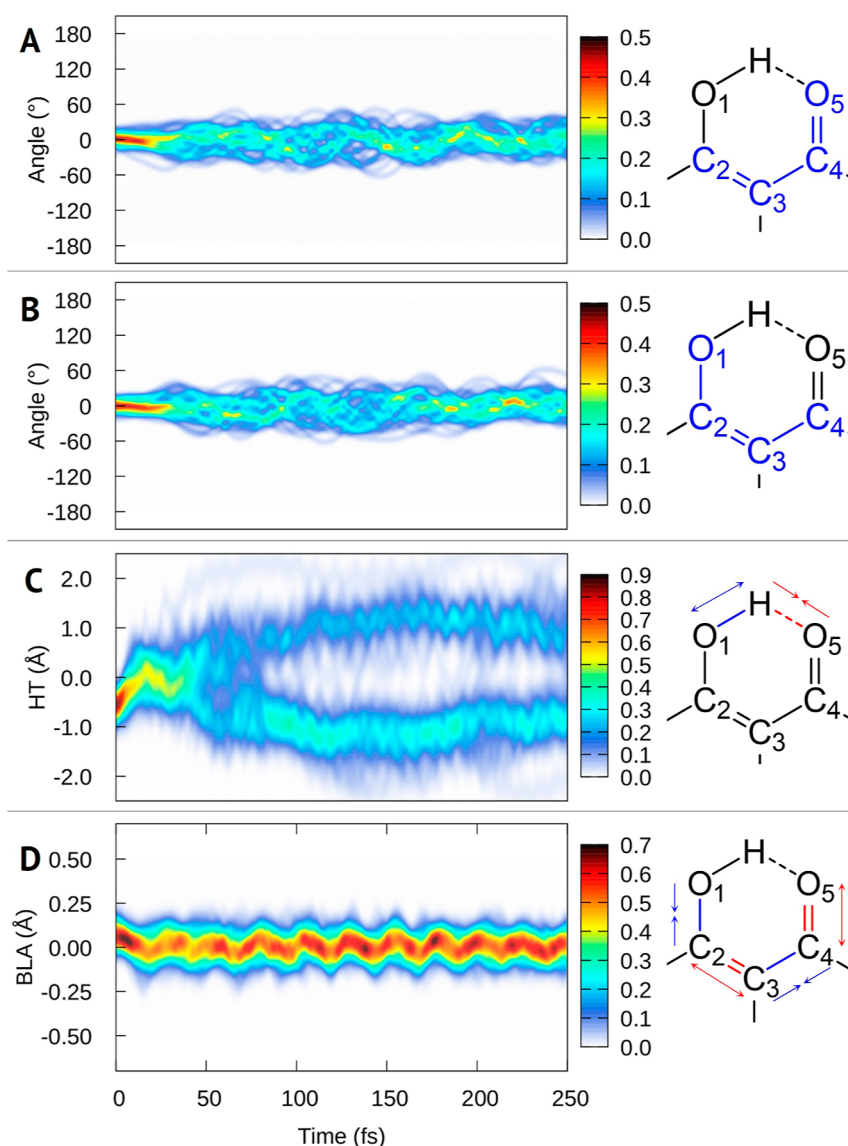


Figure 5. Coordinate densities plots over 250 fs of (A) “right” dihedral angle, (B) “left” dihedral angle, (C) hydrogen transfer (HT) coordinate $R_{O_1H} - R_{O_5H}$, (D) bond length alternation (BLA) coordinate $0.5(R_{C_2C_1} + R_{C_2O_1} - R_{C_2C_3} - R_{C_4O_5})$. On the right of each plot, the atoms involved in each motion are highlighted.

profiles (thick lines in Figure 6B,C, respectively). To highlight this resemblance the energy profiles of the active state are shown superimposed in Figure 6F. We clarify that in Figure 6F, with respect to Figure 6C, a rigid shift of 1 eV has been applied to the CASPT2 energy of the active state whenever the TDDFT active state has a $\pi\pi^*$ configuration in order to account for the strong overestimation of its energy at TDDFT level (Table 1). The resemblance between the CASPT2 and TDDFT energy profiles is encountered for most trajectories (see the Supporting Information).

Upon comprehensive comparison of both the energetics and oscillator strengths of the $\pi\pi^*$ and $n\pi^*$ states, we observe a general agreement between the SR and MR methods used in the description of the PES topologies, except for a systematic blue shift of the $\pi\pi^*$ energy at TDDFT level. This shift has an important consequence for the dynamics simulations as the larger $\pi\pi^*/n\pi^*$ gap at the LR-TDA-DFT level implies a slower $\pi\pi^* \rightarrow n\pi^*$ IC compared to simulations run at the CASPT2 level.

In the first 100 fs, we can appreciate the importance of our tool, in two different time windows, before and after the $S_2 \rightarrow S_1$ hop at 60 fs. In the first 60 fs of the TDDFT trajectory (Figure 6B), the active $\pi\pi^*$ state always corresponds to the adiabatic S_2 , which indeed does not change its character, as it can be verified by the (approximately) constant value of its oscillator strength (Figure 6A). Instead, when calculating the CASPT2 energies on top of TDDFT geometries (Figure 6C), the relative energies of the $\pi\pi^*$ and $n\pi^*$ states change several times in the early dynamics. Indeed, tracking the oscillator strengths of two states (Figure 6D), we can notice how the bright (i.e., $\pi\pi^*$) state becomes the adiabatically lowest in energy after just 5 fs. Moreover, we can notice how the relative energies of the $\pi\pi^*$ and $n\pi^*$ states are inverted four more times before the hop occurs. This means that simply matching the corresponding TDDFT and CASPT2 adiabatic states would lead to a wrong state assignment for a good part of the initial dynamics and, consequently, to an incorrect calculation of the evolution of any molecular property. Thus, the WFO analysis is able to correctly

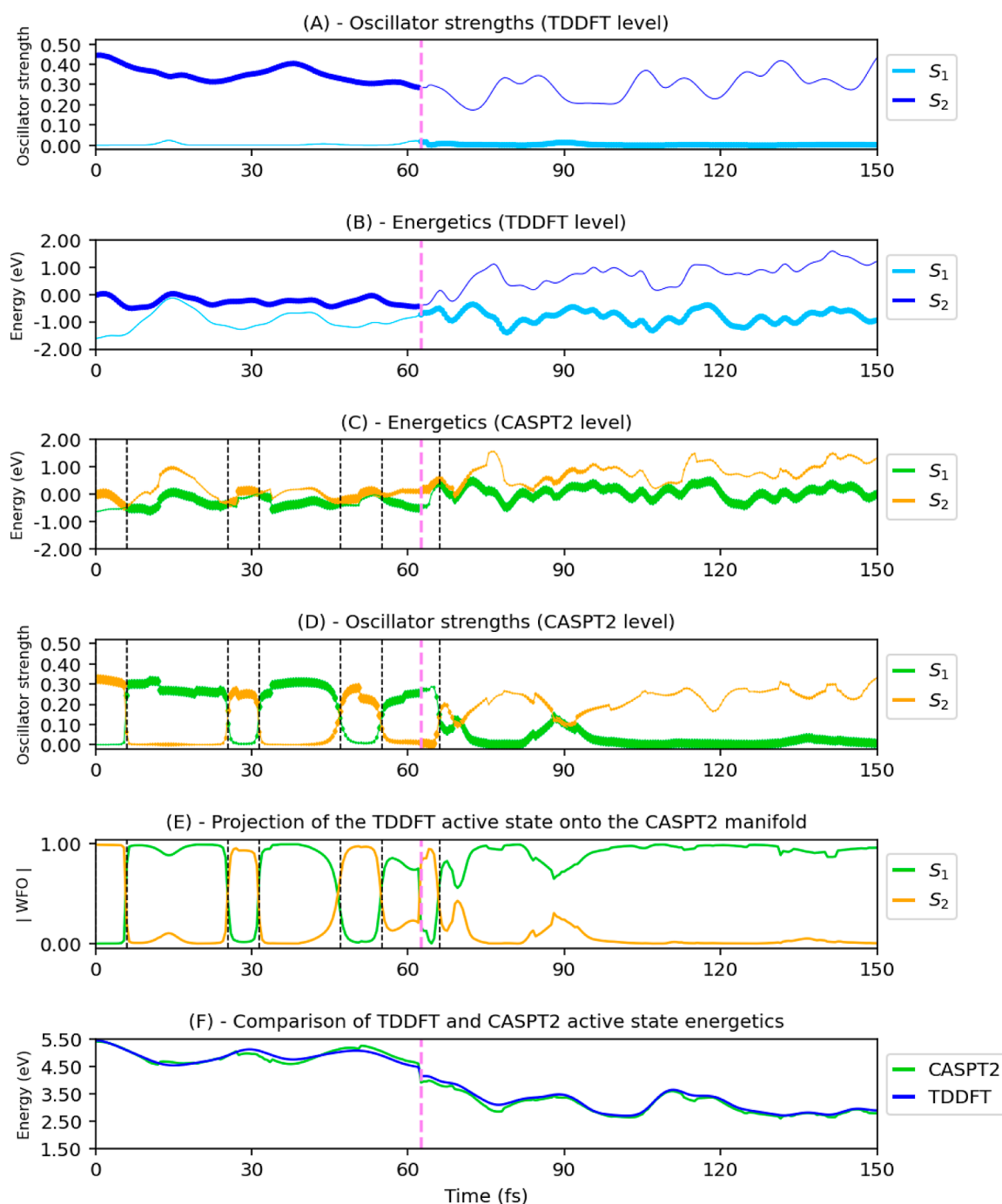


Figure 6. Sample 1—(A) oscillator strengths of the two lowest excited states over the TDDFT dynamic, highlighting the active one. (B) Energy of the three lowest excited states over the TDDFT dynamic, highlighting the active one. (C) Energy of the two lowest excited states at CASPT2 level along the TDDFT dynamic, highlighting the one with the highest overlap to the TDDFT active state. (D) Oscillator strengths of the two lowest excited states at the CASPT2 level over the TDDFT dynamic, highlighting the one with the highest overlap to the TDDFT active state. (E) Absolute value of the WFO of the first two CASPT2 excited states with the TDDFT active state. (F) Energy difference between active and ground state, computed at each level of theory. A fixed shift has been applied to account for the TDDFT overestimation of the $\pi\pi^*$ state energy. The line thickness in (C) and (D) is proportional to the projection of the TDDFT active state onto the CASPT2 manifold (E).

map the TDDFT and CASPT2 manifolds onto each other, in a fast and automatized fashion, without the need to manually compare relative energies and oscillator strengths (Figure 6E).

Figure 7 shows the same analysis for sample trajectory 2. One notes that over large segments of the simulation the bright $\pi\pi^*$ state maps onto adiabatic state S_1 at CASPT2 level following an immediate state inversion within 5 fs after photoexcitation (green thick line until 80 fs in Figure 7C,D). The WFO analysis

(Figure 7E) reveals that the 5 fs before the hop the active state begins to map onto the dark adiabatic, state S_2 at CASPT2 level (orange thick line around 80 fs in Figure 7D), thus correctly capturing the character inversion preceding the hop at TDDFT level clearly visible in the TDDFT oscillator strength profile (Figure 7A). Following the hop, the active state conserves the dark character until the end of the simulation.

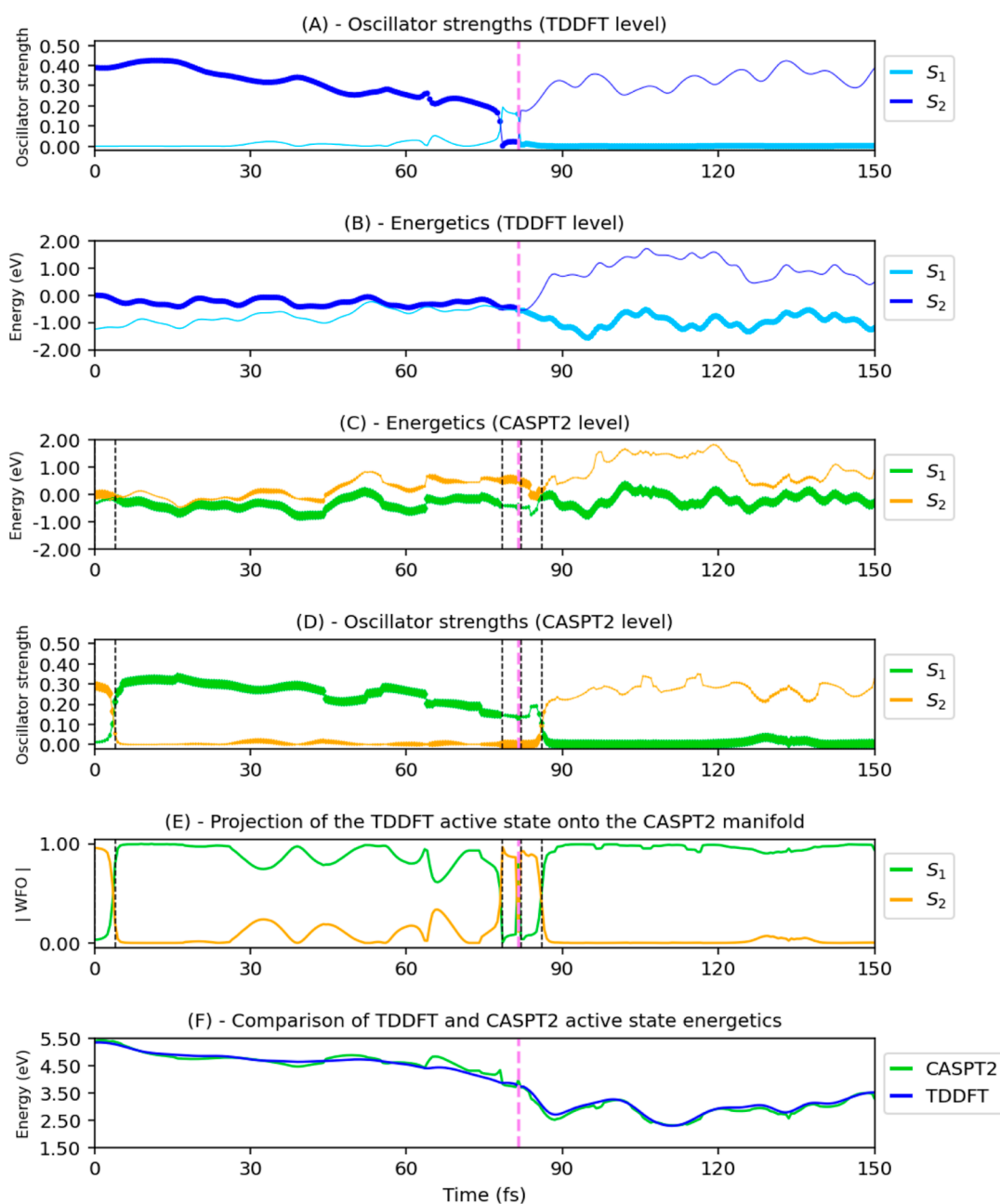


Figure 7. Sample 2—(A) oscillator strengths of the two lowest excited states over the TDDFT dynamic, highlighting the active one. (B) Energy of the three lowest excited states over the TDDFT dynamic, highlighting the active one. (C) Energy of the two lowest excited states at CASPT2 level along the TDDFT dynamic, highlighting the one with the highest overlap to the TDDFT active state. (D) Oscillator strengths of the two lowest excited states at the CASPT2 level over the TDDFT dynamic, highlighting the one with the highest overlap to the TDDFT active state. (E) Absolute value of the WFO of the first two CASPT2 excited states with the TDDFT active state. (F) Energy difference between active and ground states, computed at each level of theory. A fixed shift has been applied to account for the TDDFT overestimation of the $\pi\pi^*$ state energy. The line thickness in (C) and (D) is proportional to the projection of the TDDFT active state onto the CASPT2 manifold (E).

While in both trajectories hops occur in regions of degeneracy at the TDDFT level, the corresponding CASPT2 states are separated by a finite energy gap, a consequence of the shift between the two levels in the description of the $\pi\pi^*$ state. Under certain circumstances, such a discrepancy can have undesired consequences in the simulation of the TA spectra. For example, if the hopping occurs between two states, which are both bright from the GS, this would lead to discontinuity in the SE, which is computed relying on the CASPT2 energetics.

The use of the WFO analysis might appear redundant to the reader since we demonstrate that the same information can be

extracted from the oscillator strengths. In fact, we remind that acetylacetone is chosen precisely because oscillator strengths analysis allows us to verify the functionality of the WFO tool. In general, a system can present multiple dark and/or bright states, making it impossible to perform classification based on oscillator strengths. Moreover, the WFO analysis allows quantifying the SR-onto-MR mapping, a feature of critical importance for the calculation of spectroscopic signals (eqs 16 and 17).

3.3. Transient Absorption Simulations. The GSB, SE, and ESA contributions to the spectra are computed following eq 18, thereby relying on the definition of the projected

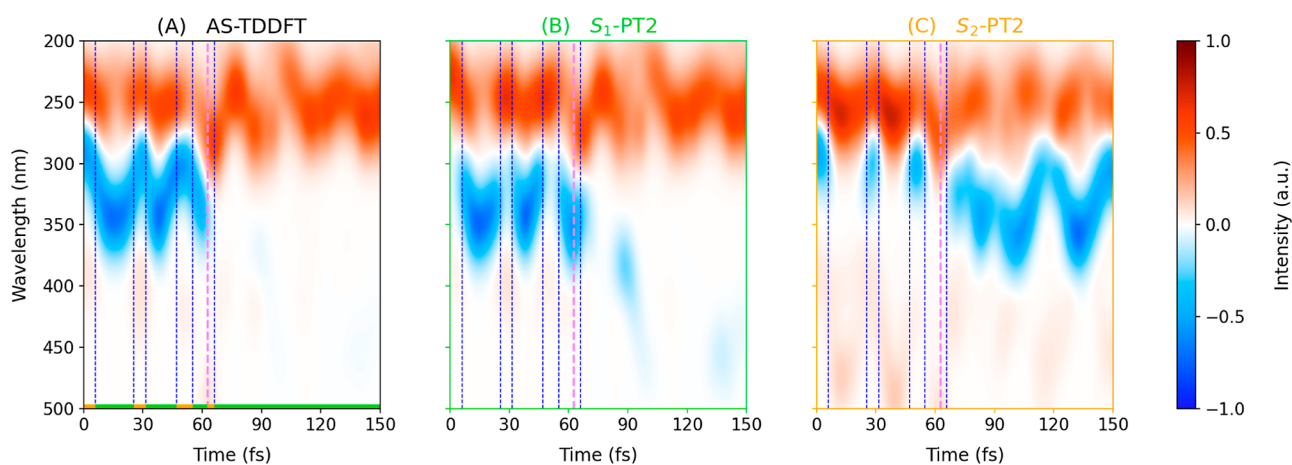


Figure 8. CASPT2 transient spectra of (A) the active TDDFT state, (B) S_1 , and (C) S_2 . Signals computed are stimulated emission (blue) and excited state absorption (dark orange). In the bottom border of the A graph, the most populated CASPT2 state is reported as an alternatively colored line.

quantities—energies and TDM—derived in eqs 16 and 17. Considering that in the time interval of interest, the absence of GS recovery yields a GSB constant contribution, we focus on the time-dependent state-specific SE and ESA features. SE can be observed only from the bright $\pi\pi^*$ state while it disappears upon decay to the $n\pi^*$ state. As shown in Table 1 each one of the two photoactive states $n\pi^*$ and $\pi\pi^*$ is dipole-coupled to a doubly excited state, of $n\pi\pi^{*2}$ and $n^0\pi^{*2}$ nature, respectively, which can be accessed through a dipole-allowed one-electron $\pi \rightarrow \pi^*$ transition. This gives rise to characteristic ESA features in the mid-UV (ca. 5.2 eV or 250 nm) blue-shifted with respect to the GSB and SE features. Notably, both ESA appear in the same spectral window and exhibit comparable oscillator strengths, with the $n\pi^*$ ESA being slightly more intense.

In Figure 8, we present the SE and ESA contributions (shown in blue and red color, respectively) from trajectory sample 1.

Figure 8 shows the spectra corresponding to sample 1 (Figure 6), generated using as a reference state for computing transition energies and TDM either the S_1 (Figure 8B) or S_2 (Figure 8C) adiabatic states at CASPT2 level. Discontinuities are present in both spectra, as visible from the SE and ESA intensities. Instead, when we use as a reference state the one indicated by the WFO analysis (Figure 6E), the spectrum improves substantially (Figure 8A). We can appreciate the high-frequency oscillation (ca. 20 fs period), a consequence of the vibrational motion. Indeed, analysis of the dynamics of representative coordinates shows that C=C and C=O stretchings are activated upon excitation.

We can note the almost instantaneous drop in intensity associated with the $S_2 \rightarrow S_1$ hop, whereas the ESA survives. As discussed above, the reason is that both $n\pi^*$ and $\pi\pi^*$ exhibit bright doubly excited states, which fall in the same spectral window around 250 nm. This complicates identifying the IC based on the ESA by visual inspection. Yet, we can notice the more pronounced quantum beating in the ESA signal after the hop, a clear indication of different vibrational dynamics activated upon IC.

Before looking at the total TA spectrum, we focus on the SE signal. The SE can straightforwardly be obtained also at the TDDFT level, as TDM from the GS are computed and stored along the dynamics. Figure 9 shows a comparison between the TDDFT and CASPT2 SE. The two features are very similar, something which can be appreciated even better in the energy domain (Figure 9)—showing an instantaneous red shift to

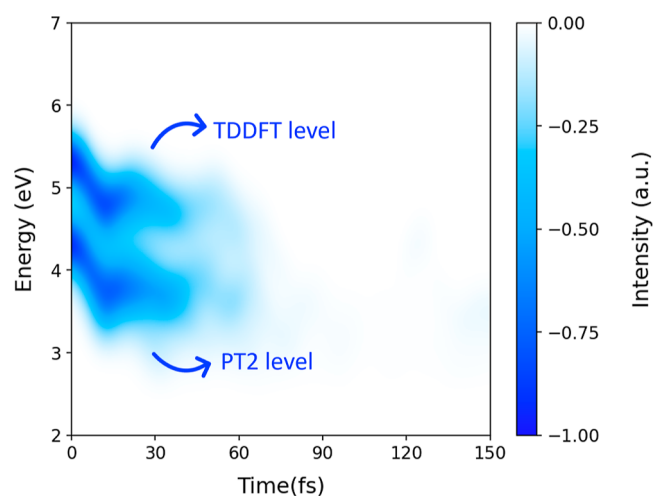


Figure 9. Stimulated emission (SE) signals computed over the TDDFT trajectory manifold. The signal at lower energy is computed at the CASPT2 level after WFO, and the one at higher energy is computed at the TDDFT level.

longer wavelengths modulated by a couple of coherent oscillations with a 20 fs period before decaying nearly completely after about 60 fs. The TDDFT signal exhibits about 45 nm blue shift, proportional to the 1 eV difference in the TDDFT and CASPT2 $\pi\pi^*$ energetics. The agreement between the two features supports the observation made earlier that TDDFT and CASPT2 predict similar PES energy profiles for the $\pi\pi^*$ state and disagree merely a constant contribution to the total energy.

The complete transient spectrum generated with the ensemble of 45 trajectories is shown in Figure 10A. In the spectral window above 250 nm, one notes a negative contribution, a combination of the SE discussed earlier and the GSB between 250 and 300 nm. The SE red shift and sub-100 fs decay lead to the depletion of the negative signal by 60% leaving visible the GSB, which survives over the entire duration of the simulation. In the window below 250 nm, one can note a positive contribution, the ESA from the active state to the dipole-coupled doubly excited states, which intensifies slightly at longer times. Both contributions are characterized by an intensity beating pattern, which can be appreciated by the time traces taken at 288 and 230 nm (Figure 10B). The two

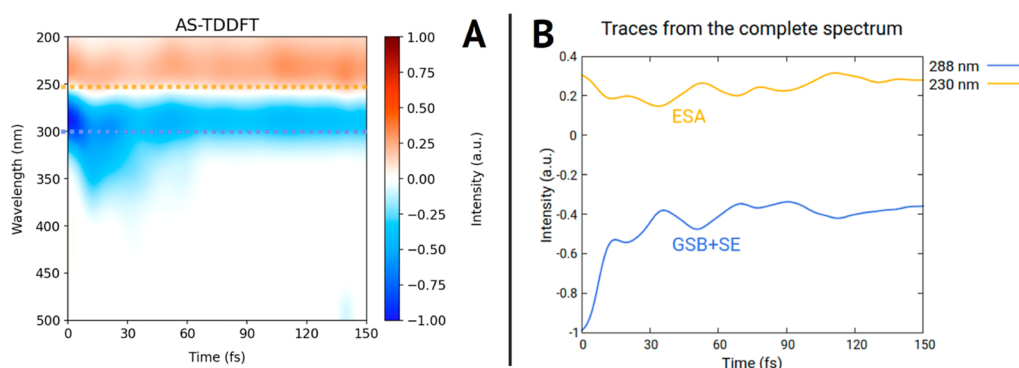


Figure 10. (A) Simulated transient absorption spectrum of AcAc obtained through averaging of 45 excited state trajectories. The signal at higher energy (dark orange) is assigned to excited state absorption (ESA), while the ones at lower energy (blue) are assigned to a combination of ground state bleaching (GSB) and stimulated emission (SE) to the ground state. (B) Values of intensity over time from the complete transient spectrum at two selected wavelengths; one for the ESA signal and one for SE and GSB signals.

traces show a complementary beating pattern. In fact, the GSB, the only contribution to the negative signal after 60 fs, is time-independent and the intensity fluctuations are caused by destructive interference with the ESA. Specifically, a red shift of the ESA toward 288 nm leads to the simultaneous intensity decrease at 230 nm and SE depletion at 288 nm due to interference.

4. CONCLUSIONS

We have presented a wave function overlap tool (WFOT) computational utility for mapping the manifolds of states of SR and MR QM electronic structure methods onto each other by means of an efficient WFO calculation. At the core of the computational protocol is a pseudounitary transformation of the manifolds of occupied and virtual MOs to maximize the overlap between the MOs in the SR and MR calculations, thereby allowing us to express the WFO as a sum over products of CI coefficients. The functionality of the WFO protocol is demonstrated for LR-TDA-DFT and XMS-CASPT2, yet the tool can already be used with variations of the family of MR methods, such as RASPT2. Moreover, future extension of the capabilities of the WFO tool toward other SR methods, whose WF can be written as a CIS-like expansion (e.g., algebraic diagrammatic construction), is straightforward. At the moment, the program is interfaced with the QM software Gaussian, NWChem, and OpenMolcas and permits the use of different basis sets in the SR and MR calculations. We have validated the WFO tool along the ultrafast $S_2 \rightarrow S_1$ IC in acetylacetone, a system that exhibits a bright $\pi\pi^*$ and a dark $n\pi^*$ states that can be conveniently tracked by means of oscillator strength analysis. Specifically, on-the-fly mixed quantum-classical dynamics is performed at the LR-TDA-DFT level of theory. Subsequently, the electronic structure at each timestep is recomputed at the XMS-CASPT2 level of theory. The WFO tool is then used to map the TDDFT photoactive state onto the CASPT2 manifold allowing to track its nature throughout the dynamics. The WFO presented analysis is perfectly general and allows state tracking also in case of multiple spectroscopically dark and/or bright states where the oscillator strength analysis would fail.

Our model system, acetylacetone, exhibits a significant disparity in the energetics of the $\pi\pi^*$ configuration between LR-TDA-DFT and XMS-CASPT2. While CASPT2 slightly underestimates its energy, TDDFT notably overestimates it relative to experimental data. The aim of the current work is not to assess the quality of either method but rather to demonstrate

the capacity of the WFO tool. Nevertheless, we emphasize that the accuracy of any observable depends on the reliability of the electronic structure method used to compute it. Therefore, we recommend validating both SR and MR methods through preliminary static calculations at key critical points. The WFO tool can be immensely valuable in this endeavor, as it aids in identifying electronic states not reproduced at the SR level of theory such as lower-lying doubly excited states. These states typically exhibit WFO values close to zero.

Besides the already mentioned extension to other SR methods, the WFO analysis can be generalized to map different SR (or MR) methods onto each other. In particular, mapping of CASPT2 calculations with active spaces of arbitrary size/composition would allow us to automatize the calculation of spectroscopic observables on top of on-the-fly dynamics simulations. Another highly compelling application involves leveraging the WFO tool for the potential development of machine-learned DFT functionals aimed at achieving MR accuracy in correlation treatment.^{69,70}

The WFO has been integrated in the COBRAMM suite. This makes possible the simulation of various types of electronic spectroscopies such as transient absorption, photoemission, and X-ray, using MR methods on top of on-the-fly dynamics carried out with SR methods, thereby combining the computational efficiency of SR methods and the spectrum completeness of MR methods. Remarkably, the ESA features in the TA absorption spectrum of acetylacetone arise from dipole-allowed one-electron $\pi \rightarrow \pi^*$ transition from the photoactive states to higher lying doubly excited states, which are beyond the scope of LR-TDA-DFT.

Regarding spectroscopy simulations, we emphasize that while MR methods are required to provide a complete manifold of spectroscopic signals, the temporal evolution of spectral features—i.e., the time scales at which these features emerge or decay—hinges on the accuracy of the underpinning SR dynamics. Thus, the WFO tool offers a valuable protocol for validating the SR dynamics against experiment by computing an observable such as the transient spectrum.

■ ASSOCIATED CONTENT

Supporting Information

The Supporting Information is available free of charge at <https://pubs.acs.org/doi/10.1021/acs.jctc.4c00310>.

Molecular orbitals of the active space of the CASPT2 calculations; comparison of energetics and oscillator

strengths at the CASPT2 and TDDFT levels and mapping the TDDFT active state onto the CASPT2 manifold for 10 exemplary trajectories of the dynamics; simulated transient absorption spectrum without the GSB component; and benchmark of several TDDFT functionals in the Franck–Condon point (PDF)

AUTHOR INFORMATION

Corresponding Authors

Marco Garavelli – Dipartimento di Chimica Industriale “Toso Montanari”, University of Bologna, Bologna 40129, Italy;

orcid.org/0000-0002-0796-289X;

Email: marco.garavelli@unibo.it

Niranjan Govind – Physical and Computational Sciences Directorate, Pacific Northwest National Laboratory, Richland, Washington 99352, United States; Department of Chemistry, University of Washington, Seattle, Washington 98195, United States; orcid.org/0000-0003-3625-366X;

Email: niri.govind@pnnl.gov

Artur Nenov – Dipartimento di Chimica Industriale “Toso Montanari”, University of Bologna, Bologna 40129, Italy;

orcid.org/0000-0003-3071-5341; Email: artur.nenov@

unibo.it

Authors

Alessandro Loreti – Dipartimento di Chimica Industriale “Toso Montanari”, University of Bologna, Bologna 40129, Italy; orcid.org/0009-0002-6958-7324

Victor Manuel Freixas – Department of Chemistry and Department of Physics and Astronomy, University of California, Irvine, California 92697, United States; orcid.org/0000-0003-1733-4827

Davide Avagliano – Dipartimento di Chimica Industriale “Toso Montanari”, University of Bologna, Bologna 40129, Italy; Present Address: Institute of Chemistry for Life and Health Sciences (I-CLEHS) Chimie Paristech, 11 Rue Pierre et Marie Curie, 75005, Paris, France; orcid.org/0000-0001-5539-9731

Francesco Segatta – Dipartimento di Chimica Industriale “Toso Montanari”, University of Bologna, Bologna 40129, Italy; orcid.org/0000-0003-4150-6676

Huajing Song – Physics and Chemistry of Materials, Theoretical Division, Los Alamos National Laboratory, Los Alamos, New Mexico 87545, United States; Present Address: Materials and Process Engineering, Pratt and Whitney, Raytheon Technologies, East Hartford, CT 06118, USA; orcid.org/0000-0001-5958-7377

Sergei Tretiak – Physics and Chemistry of Materials, Theoretical Division, Los Alamos National Laboratory, Los Alamos, New Mexico 87545, United States; Center for Integrated Nanotechnologies, Los Alamos National Laboratory, Los Alamos, New Mexico 87545, United States; orcid.org/0000-0001-5547-3647

Shaul Mukamel – Department of Chemistry and Department of Physics and Astronomy, University of California, Irvine, California 92697, United States; orcid.org/0000-0002-6015-3135

Complete contact information is available at:
<https://pubs.acs.org/10.1021/acs.jctc.4c00310>

Notes

The authors declare no competing financial interest.

ACKNOWLEDGMENTS

This study was supported by the U.S. Department of Energy, Office of Science, Office of Basic Energy Sciences, Division of Chemical Sciences, Geosciences, and Biosciences under DE-SC0022225 (V.M.F., S.M. at the University of California, Irvine and F.S., M.G., A.N. at the University of Bologna, Italy) and FWP 72684 (N.G. at the Pacific Northwest National Laboratory (PNNL)). The research was performed in part at the Center for Integrated Nanotechnologies (CINT), a U.S. Department of Energy, Office of Science user facility at Los Alamos National Laboratory (LANL). This work benefited from computational resources provided by the National Energy Research Scientific Computing Center (NERSC), a U.S. Department of Energy Office of Science User Facility operated under contract no. DE-AC02-05CH11231 and computational resources provided by EMSL, a DOE Office of Science User Facility sponsored by the Office of Biological and Environmental Research and located at PNNL. PNNL is operated by Battelle Memorial Institute for the United States Department of Energy under DOE contract no. DE-AC05-76RL1830.

ADDITIONAL NOTES

“Notable exceptions have been identified for extended conjugated and aromatic organic molecules (and aggregates thereof) where low-lying doubly excited states are involved in the energy conversion.¹¹”

^bOne can use the off-diagonal blocks of the MO overlap matrix as a diagnostic tool regarding the validity of the assumption.

^cWFO analysis of TDDFT and CASPT2 calculations performed with different basis sets is currently possible only through the interface with COBRAMM.

REFERENCES

- (1) Casida, M.; Huix-Rotllant, M. Progress in Time-Dependent Density-Functional Theory. *Annu. Rev. Phys. Chem.* **2012**, *63*, 287–323.
- (2) Liang, J.; Feng, X.; Hait, D.; Head-Gordon, M. Revisiting the Performance of Time-Dependent Density Functional Theory for Electronic Excitations: Assessment of 43 Popular and Recently Developed Functionals from Rungs One to Four. *J. Chem. Theory Comput.* **2022**, *18*, 3460–3473.
- (3) Tully, J. C. Molecular dynamics with electronic transitions. *J. Chem. Phys.* **1990**, *93*, 1061–1071.
- (4) Subotnik, J. E.; Jain, A.; Landry, B.; Petit, A.; Ouyang, W.; Bellonzi, N. Understanding the Surface Hopping View of Electronic Transitions and Decoherence. *Annu. Rev. Phys. Chem.* **2016**, *67*, 387–417.
- (5) Mai, S.; Marquetand, P.; González, L. *Surface Hopping Molecular Dynamics*; John Wiley & Sons, Ltd, 2020; Chapter 16, pp 499–530.
- (6) Jain, A.; Sindhu, A. Pedagogical Overview of the Fewest Switches Surface Hopping Method. *ACS Omega* **2022**, *7*, 45810–45824.
- (7) Elliott, P.; Goldson, S.; Canahui, C.; Maitra, N. T. Perspectives on double-excitations in TDDFT. *Chem. Phys.* **2011**, *391*, 110–119.
- (8) Maitra, N. T. Double and Charge-Transfer Excitations in Time-Dependent Density Functional Theory. *Annu. Rev.* **2022**, *73*, 117–140.
- (9) Szabo, A.; Ostlund, N. S. *Modern Quantum Chemistry: Introduction to Advanced Electronic Structure Theory*; Courier Corporation, 2012.
- (10) Levine, B. G.; Ko, C.; Quenneville, J.; Martínez, T. J. Conical intersections and double excitations in time-dependent density functional theory. *Mol. Phys.* **2006**, *104*, 1039–1051.
- (11) do Casal, M. T.; Toldo, J. M.; Barbatti, M.; Plasser, F. Classification of doubly excited molecular electronic states. *Chem. Sci.* **2023**, *14*, 4012–4026.
- (12) Maitra, N. T.; Zhang, F.; Cave, R. J.; Burke, K. Double excitations within time-dependent density functional theory linear response. *J. Chem. Phys.* **2004**, *120*, 5932–5937.

- (13) Cave, R. J.; Zhang, F.; Maitra, N. T.; Burke, K. A dressed TDDFT treatment of the 21Ag states of butadiene and hexatriene. *Chem. Phys. Lett.* **2004**, *389*, 39–42.
- (14) Mazur, G.; Makowski, M.; Włodarczyk, R.; Aoki, Y. Dressed TDDFT study of low-lying electronic excited states in selected linear polyenes and diphenylpolyenes. *Int. J. Quantum Chem.* **2011**, *111*, 819–825.
- (15) Huix-Rotllant, M.; Ipatov, A.; Rubio, A.; Casida, M. E. Assessment of dressed time-dependent density-functional theory for the low-lying valence states of 28 organic chromophores. *Chem. Phys.* **2011**, *391*, 120–129.
- (16) Horbatenko, Y.; Sadiq, S.; Lee, S.; Filatov, M.; Choi, C. H. Mixed-Reference Spin-Flip Time-Dependent Density Functional Theory (MRSF-TDDFT) as a Simple yet Accurate Method for Diradicals and Diradicaloids. *J. Chem. Theory Comput.* **2021**, *17*, 848–859.
- (17) Seidu, I.; Krykunov, M.; Ziegler, T. The formulation of a constricted variational density functional theory for double excitations. *Mol. Phys.* **2014**, *112*, 661–668.
- (18) Hait, D.; Head-Gordon, M. Orbital Optimized Density Functional Theory for Electronic Excited States. *J. Phys. Chem. Lett.* **2021**, *12*, 4517–4529.
- (19) Lykos, P. G.; Schmeising, H. N. Maximum overlap atomic and molecular orbitals. *J. Chem. Phys.* **1961**, *35*, 288–293.
- (20) King, H. F.; Stanton, R. E.; Kim, H.; Wyatt, R. E.; Parr, R. G. Corresponding orbitals and the nonorthogonality problem in molecular quantum mechanics. *J. Chem. Phys.* **1967**, *47*, 1936–1941.
- (21) Gilbert, A. T. B.; Besley, N. A.; Gill, P. M. W. Self-Consistent Field Calculations of Excited States Using the Maximum Overlap Method (MOM). *J. Phys. Chem. A* **2008**, *112*, 13164–13171.
- (22) Segatta, F.; Russo, M.; Nascimento, D. R.; Presti, D.; Rigodanza, F.; Nenov, A.; Bonvicini, A.; Arcioni, A.; Mukamel, S.; Maiuri, M.; Muccioli, L.; Govind, N.; Cerullo, G.; Garavelli, M. In Silico Ultrafast Nonlinear Spectroscopy Meets Experiments: The Case of Perylene Bisimide Dye. *J. Chem. Theory Comput.* **2021**, *17*, 7134–7145.
- (23) Li, S. L.; Marenich, A. V.; Xu, X.; Truhlar, D. G. Configuration interaction-corrected Tamm–Dancoff approximation: A time-dependent density functional method with the correct dimensionality of conical intersections. *J. Phys. Chem. Lett.* **2014**, *5*, 322–328.
- (24) Shu, Y.; Parker, K. A.; Truhlar, D. G. Dual-functional Tamm–Dancoff approximation with self-interaction-free orbitals: vertical excitation energies and potential energy surfaces near an intersection seam. *J. Phys. Chem. A* **2017**, *121*, 9728–9735.
- (25) Teh, H.-H.; Subotnik, J. E. The simplest possible approach for simulating S₀–S₁ conical intersections with DFT/TDDFT: Adding one doubly excited configuration. *J. Phys. Chem. Lett.* **2019**, *10*, 3426–3432.
- (26) Athavale, V.; Teh, H.-H.; Shao, Y.; Subotnik, J. Analytical gradients and derivative couplings for the TDDFT-1D method. *J. Chem. Phys.* **2022**, *157*, 244110.
- (27) Nenov, A.; Borrego-Varillas, R.; Oriana, A.; Ganzer, L.; Segatta, F.; Conti, I.; Segarra-Martí, J.; Omachi, J.; Dapor, M.; Taioli, S.; Manzoni, C.; Mukamel, S.; Cerullo, G.; Garavelli, M. UV-Light-Induced Vibrational Coherences: The Key to Understand Kasha Rule Violation in trans-Azobenzene. *J. Phys. Chem. Lett.* **2018**, *9*, 1534–1541.
- (28) Borrego-Varillas, R.; Nenov, A.; Kabaciński, P.; Conti, I.; Ganzer, L.; Oriana, A.; Jaiswal, V. K.; Delfino, I.; Weingart, O.; Manzoni, C.; Rivalta, I.; Garavelli, M.; Cerullo, G. Tracking excited state decay mechanisms of pyrimidine nucleosides in real time. *Nat. Commun.* **2021**, *12*, 7285.
- (29) Nenov, A.; Giussani, A.; Fingerhut, B. P.; Rivalta, I.; Dumont, E.; Mukamel, S.; Garavelli, M. Spectral lineshapes in nonlinear electronic spectroscopy. *Phys. Chem. Chem. Phys.* **2015**, *17*, 30925–30936.
- (30) Jaiswal, V. K.; Kabaciński, P.; Nogueira de Faria, B. E.; Gentile, M.; de Paula, A. M.; Borrego-Varillas, R.; Nenov, A.; Conti, I.; Cerullo, G.; Garavelli, M. Environment-Driven Coherent Population Transfer Governs the Ultrafast Photophysics of Tryptophan. *J. Am. Chem. Soc.* **2022**, *144*, 12884–12892.
- (31) Mai, S.; Marquetand, P.; González, L. Intersystem Crossing Pathways in the Noncanonical Nucleobase 2-Thiouracil: A Time-Dependent Picture. *J. Phys. Chem. Lett.* **2016**, *7*, 1978–1983.
- (32) Manathunga, M.; Yang, X.; Luk, H. L.; Gozem, S.; Frutos, L. M.; Valentini, A.; Ferrè, N.; Olivucci, M. Probing the Photodynamics of Rhodopsins with Reduced Retinal Chromophores. *J. Chem. Theory Comput.* **2016**, *12*, 839–850.
- (33) Borrego-Varillas, R.; Teles-Ferreira, D. C.; Nenov, A.; Conti, I.; Ganzer, L.; Manzoni, C.; Garavelli, M.; Maria de Paula, A.; Cerullo, G. Observation of the Sub-100 Femtosecond Population of a Dark State in a Thiobase Mediating Intersystem Crossing. *J. Am. Chem. Soc.* **2018**, *140*, 16087–16093.
- (34) Polyak, I.; Hutton, L.; Crespo-Otero, R.; Barbatti, M.; Knowles, P. J. Ultrafast Photoinduced Dynamics of 1,3-Cyclohexadiene Using XMS-CASPT2 Surface Hopping. *J. Chem. Theory Comput.* **2019**, *15*, 3929–3940.
- (35) Travníkova, O.; Piteša, T.; Ponzi, A.; Sapunar, M.; Squibb, R. J.; Richter, R.; Finetti, P.; Di Fraia, M.; De Fanis, A.; Mahne, N.; Manfreda, M.; Zhaunerchyk, V.; Marchenko, T.; Guillemin, R.; Journal, L.; Prince, K. C.; Callegari, C.; Simon, M.; Feifel, R.; Decleva, P.; Došlić, N.; Piancastelli, M. N. Photochemical Ring-Opening Reaction of 1,3-Cyclohexadiene: Identifying the True Reactive State. *J. Am. Chem. Soc.* **2022**, *144*, 21878–21886.
- (36) Gil, E. S.; de Araújo, B. B.; Gonçalves, P. F. B. CASPT2, CASSCF and non-adiabatic molecular dynamics (NAMD) studies on the low-lying electronic states of 1H-1,2,3-triazole photolysis. *Phys. Chem. Chem. Phys.* **2019**, *21*, 25809–25819.
- (37) Xu, C.; Lin, K.; Hu, D.; Gu, F. L.; Gelin, M. F.; Lan, Z. Ultrafast Internal Conversion Dynamics through the on-the-Fly Simulation of Transient Absorption Pump–Probe Spectra with Different Electronic Structure Methods. *J. Phys. Chem. Lett.* **2022**, *13*, 661–668.
- (38) Chakraborty, P.; Liu, Y.; Weinacht, T.; Matsika, S. Effect of dynamic correlation on the ultrafast relaxation of uracil in the gas phase. *Faraday Discuss.* **2021**, *228*, 266–285.
- (39) Park, J. W.; Shiozaki, T. On-the-Fly CASPT2 Surface-Hopping Dynamics. *J. Chem. Theory Comput.* **2017**, *13*, 3676–3683.
- (40) Buchner, F.; Nakayama, A.; Yamazaki, S.; Ritze, H.-H.; Lübbcke, A. Excited-State Relaxation of Hydrated Thymine and Thymidine Measured by Liquid-Jet Photoelectron Spectroscopy: Experiment and Simulation. *J. Am. Chem. Soc.* **2015**, *137*, 2931–2938.
- (41) Valiev, M.; Bylaska, E. J.; Govind, N.; Kowalski, K.; Straatsma, T. P.; Van Dam, H. J.; Wang, D.; Nieplocha, J.; Aprà, E.; Windus, T. L.; et al. NWChem: A comprehensive and scalable open-source solution for large scale molecular simulations. *Comput. Phys. Commun.* **2010**, *181*, 1477–1489.
- (42) Aprà, E.; Bylaska, E. J.; De Jong, W. A.; Govind, N.; Kowalski, K.; Straatsma, T. P.; Valiev, M.; van Dam, H.; Alexeev, Y.; Anchell, J.; et al. NWChem: Past, present, and future. *J. Chem. Phys.* **2020**, *152*, 184102.
- (43) Mejia-Rodriguez, D.; Aprà, E.; Autschbach, J.; Bauman, N. P.; Bylaska, E. J.; Govind, N.; Hammond, J. R.; Kowalski, K.; Kunitsa, A.; Panyala, A.; et al. NWChem: Recent and Ongoing Developments. *J. Chem. Theory Comput.* **2023**, *19*, 7077–7096.
- (44) Frisch, M. J.; Trucks, G. W.; Schlegel, H. B.; Scuseria, G. E.; Robb, M. A.; Cheeseman, J. R.; Scalmani, G.; Barone, V.; Petersson, G. A.; Nakatsuji, H.; Li, X.; Caricato, M.; Marenich, A. V.; Bloino, J.; Janesko, B. G.; Gomperts, R.; Mennucci, B.; Hratchian, H. P.; Ortiz, J. V.; Izmaylov, A. F.; Sonnenberg, J. L.; Williams-Young, D.; Ding, F.; Lipparini, F.; Egidi, F.; Goings, J.; Peng, B.; Petrone, A.; Henderson, T.; Ranasinghe, D.; Zakrzewski, V. G.; Gao, J.; Rega, N.; Zheng, G.; Liang, W.; Hada, M.; Ehara, M.; Toyota, K.; Fukuda, R.; Hasegawa, J.; Ishida, M.; Nakajima, T.; Honda, Y.; Kitao, O.; Nakai, H.; Vreven, T.; Throssell, K.; Montgomery, J. A., Jr.; Peralta, J. E.; Ogliaro, F.; Bearpark, M. J.; Heyd, J. J.; Brothers, E. N.; Kudin, K. N.; Staroverov, V. N.; Keith, T. A.; Kobayashi, R.; Normand, J.; Raghavachari, K.; Rendell, A. P.; Burant, J. C.; Iyengar, S. S.; Tomasi, J.; Cossi, M.; Millam, J. M.; Klene, M.; Adamo, C.; Cammi, R.; Ochterski, J. W.; Martin, R. L.; Morokuma, K.; Farkas, O.; Foresman, J. B.; Fox, D. J. *Gaussian 16 Revision C.01*; Gaussian Inc.: Wallingford CT, 2016.

- (45) Aquilante, F.; Autschbach, J.; Baiardi, A.; Battaglia, S.; Borin, V. A.; Chibotaru, L. F.; Conti, I.; De Vico, L.; Delcey, M.; Fdez Galván, I.; Ferré, N.; Freitag, L.; Garavelli, M.; Gong, X.; Knecht, S.; Larsson, E. D.; Lindh, R.; Lundberg, M.; Malmqvist, P. Å.; Nenov, A.; Norell, J.; Odelius, M.; Olivucci, M.; Pedersen, T. B.; Pedraza-González, L.; Phung, Q. M.; Pierloot, K.; Reiher, M.; Schapiro, I.; Segarra-Martí, J.; Segatta, F.; Seijo, L.; Sen, S.; Sergentu, D.-C.; Stein, C. J.; Ungur, L.; Vacher, M.; Valentini, A.; Veryazov, V. Modern quantum chemistry with [Open]Molcas. *J. Chem. Phys.* **2020**, *152*, 214117.
- (46) Li Manni, G.; Fdez Galván, I.; Alavi, A.; Aleotti, F.; Aquilante, F.; Autschbach, J.; Avagliano, D.; Baiardi, A.; Bao, J. J.; Battaglia, S.; Birnoschi, L.; Blanco-González, A.; Bokarev, S. I.; Broer, R.; Cacciari, R.; Calio, P. B.; Carlson, R. K.; Carvalho Couto, R.; Cerdán, L.; Chibotaru, L. F.; Chilton, N. F.; Church, J. R.; Conti, I.; Coriani, S.; Cuéllar-Zuquin, J.; Daoud, R. E.; Dattani, N.; Decleva, P.; de Graaf, C.; Delcey, M. G.; De Vico, L.; Dobrutz, W.; Dong, S. S.; Feng, R.; Ferré, N.; Filatov, M.; Gagliardi, L.; Garavelli, M.; González, L.; Guan, Y.; Guo, M.; Hennefarth, M. R.; Hermes, M. R.; Hoyer, C. E.; Huix-Rotlant, M.; Jaiswal, V. K.; Kaiser, A.; Kaliakin, D. S.; Khamesian, M.; King, D. S.; Kochetov, V.; Krošnicki, M.; Kumaar, A. A.; Larsson, E. D.; Lehtola, S.; Lepetit, M.-B.; Lischka, H.; López Ríos, P.; Lundberg, M.; Ma, D.; Mai, S.; Marquetand, P.; Merritt, I. C. D.; Montorsi, F.; Mörchen, M.; Nenov, A.; Nguyen, V. H. A.; Nishimoto, Y.; Oakley, M. S.; Olivucci, M.; Oppel, M.; Padula, D.; Pandharkar, R.; Phung, Q. M.; Plasser, F.; Raggi, G.; Rebolini, E.; Reiher, M.; Rivalta, I.; Roca-Sanjuán, D.; Romig, T.; Safari, A. A.; Sánchez-Mansilla, A.; Sand, A. M.; Schapiro, I.; Scott, T. R.; Segarra-Martí, J.; Segatta, F.; Sergentu, D.-C.; Sharma, P.; Shepard, R.; Shu, Y.; Staab, J. K.; Straatsma, T. P.; Sørensen, L. K.; Tenorio, B. N. C.; Truhlar, D. G.; Ungur, L.; Vacher, M.; Veryazov, V.; Vofsi, T. A.; Weser, O.; Wu, D.; Yang, X.; Yarkony, D.; Zhou, C.; Zobel, J. P.; Lindh, R. The OpenMolcas Web: A Community-Driven Approach to Advancing Computational Chemistry. *J. Chem. Theory Comput.* **2023**, *19*, 6933–6991.
- (47) Chen, X.-B.; Fang, W.-H.; Phillips, D. L. Theoretical Studies of the Photochemical Dynamics of Acetylacetone: Isomerization, Dissociation, and Dehydration Reactions. *J. Phys. Chem. A* **2006**, *110*, 4434–4441.
- (48) Bhattacherjee, A.; Pemmaraju, C. D.; Schnorr, K.; Attar, A. R.; Leone, S. R. Ultrafast Intersystem Crossing in Acetylacetone via Femtosecond X-ray Transient Absorption at the Carbon K-Edge. *J. Am. Chem. Soc.* **2017**, *139*, 16576–16583.
- (49) Verma, P. K.; Koch, F.; Steinbacher, A.; Nuernberger, P.; Brixner, T. Ultrafast UV-Induced Photoisomerization of Intramolecularly H-Bonded Symmetric β -Diketones. *J. Am. Chem. Soc.* **2014**, *136*, 14981–14989.
- (50) Squibb, R. J.; Sapunar, M.; Ponzi, A.; Richter, R.; Kivimäki, A.; Plekan, O.; Finetti, P.; Sisourat, N.; Zhaunerchyk, V.; Marchenko, T.; Journel, L.; Guillemin, R.; Cucini, R.; Coreno, M.; Grazioli, C.; Di Fraia, M.; Callegari, C.; Prince, K. C.; Decleva, P.; Simon, M.; Eland, J. H. D.; Došlić, N.; Feifel, R.; Piancastelli, M. N. Acetylacetone photodynamics at a seeded free-electron laser. *Nat. Commun.* **2018**, *9*, 63.
- (51) Poisson, L.; Roubin, P.; Coussan, S.; Soep, B.; Mestdagh, J.-M. Ultrafast Dynamics of Acetylacetone (2,4-Pentanedione) in the S2 State. *J. Am. Chem. Soc.* **2008**, *130*, 2974–2983.
- (52) Finley, J.; Malmqvist, P. Å.; Roos, B. O.; Serrano-Andrés, L. The multi-state CASPT2 method. *Chem. Phys. Lett.* **1998**, *288*, 299–306.
- (53) Granovsky, A. A. Extended multi-configuration quasi-degenerate perturbation theory: The new approach to multi-state multi-reference perturbation theory. *J. Chem. Phys.* **2011**, *134*, 214113.
- (54) Shiozaki, T.; Györfy, W.; Celani, P.; Werner, H.-J. Communication: Extended multi-state complete active space second-order perturbation theory: Energy and nuclear gradients. *J. Chem. Phys.* **2011**, *135*, 081106.
- (55) Battaglia, S.; Lindh, R. Extended Dynamically Weighted CASPT2: The Best of Two Worlds. *J. Chem. Theory Comput.* **2020**, *16*, 1555–1567.
- (56) Battaglia, S.; Lindh, R. On the role of symmetry in XDW-CASPT2. *J. Chem. Phys.* **2021**, *154*, 034102.
- (57) Plasser, F.; Ruckebauer, M.; Mai, S.; Oppel, M.; Marquetand, P.; González, L. Efficient and Flexible Computation of Many-Electron Wave Function Overlaps. *J. Chem. Theory Comput.* **2016**, *12*, 1207–1219.
- (58) Malmqvist, P. Å.; Roos, B. O. The CASSCF state interaction method. *Chem. Phys. Lett.* **1989**, *155*, 189–194.
- (59) Ryabinkin, I. G.; Nagesh, J.; Izmaylov, A. F. Fast Numerical Evaluation of Time-Derivative Nonadiabatic Couplings for Mixed Quantum–Classical Methods. *J. Phys. Chem. Lett.* **2015**, *6*, 4200–4203.
- (60) Avagliano, D.; Bonfanti, M.; Nenov, A.; Garavelli, M. Automated protocol and interface to simulate QM/MM time-resolved transient absorption at TD-DFT level with COBRAMM. *J. Comput. Chem.* **2022**, *43*, 1641–1655.
- (61) Matsika, S. Three-State Conical Intersections in Nucleic Acid Bases. *J. Phys. Chem. A* **2005**, *109*, 7538–7545.
- (62) Weingart, O.; Nenov, A.; Altoè, P.; Rivalta, I.; Segarra-Martí, J.; Dokukina, I.; Garavelli, M. COBRAMM 2.0 — A software interface for tailoring molecular electronic structure calculations and running nanoscale (QM/MM) simulations. *J. Mol. Model.* **2018**, *24*, 271.
- (63) Case, D.; Ben-Shalom, I.; Brozell, S.; Cerutti, D.; Cheatham, T.; Cruzeiro, V.; Darden, T.; Duke, R.; Ghoreishi, D.; Gilson, M.; Gohlke, H.; Götz, A.; Greene, D.; Harris, R.; Homeyer, N.; Huang, Y.; Izadi, S.; Kovalenko, A.; Kurtzman, T.; Kollman, P. *AMBER 2018*; University of California: San Francisco, 2018.
- (64) Segatta, F.; Nenov, A.; Nascimento, D. R.; Govind, N.; Mukamel, S.; Garavelli, M. iSPECTRON: A simulation interface for linear and nonlinear spectra with ab-initio quantum chemistry software. *J. Comput. Chem.* **2021**, *42*, 644–659.
- (65) Pritchard, B. P.; Altarawy, D.; Didier, B.; Gibson, T. D.; Windus, T. L. New Basis Set Exchange: An Open, Up-to-Date Resource for the Molecular Sciences Community. *J. Chem. Inf. Model.* **2019**, *59*, 4814–4820.
- (66) Folkenet, M. M.; Weiss-Lopez, B. E.; Chauvel, J. P. J.; True, N. S. Gas-phase proton NMR studies of keto-enol tautomerism of acetylacetone, methyl acetoacetate, and ethyl acetoacetate. *J. Phys. Chem.* **1985**, *89*, 3347–3352.
- (67) Nakanishi, H.; Morita, H.; Nagakura, S. Electronic Structures and Spectra of the Keto and Enol Forms of Acetylacetone. *Bull. Chem. Soc. Jpn.* **1977**, *50*, 2255–2261.
- (68) List, N. H.; Dempwolff, A. L.; Dreuw, A.; Norman, P.; Martínez, T. J. Probing competing relaxation pathways in malonaldehyde with transient X-ray absorption spectroscopy. *Chem. Sci.* **2020**, *11*, 4180–4193.
- (69) Kalita, B.; Li, L.; McCarty, R. J.; Burke, K. Learning to Approximate Density Functionals. *Acc. Chem. Res.* **2021**, *54*, 818–826.
- (70) Avagliano, D.; Skreta, M.; Arellano-Rubach, S.; Aspuru-Guzik, A. DELFI: A computer oracle for recommending density functionals for excited states calculations. *Chem. Sci.* **2024**, *15*, 4489–4503.

Supporting information - WFOT: a WaveFunction Overlap Tool Between Single- and Multi-Reference Electronic Structure Methods for Spectroscopy Simulation

Alessandro Loreti,[†] Victor Manuel Freixas,[‡] Davide Avagliano,^{†,#} Francesco Segatta,[†] Huajing Song,^{¶,@} Sergei Tretiak,^{¶,§} Shaul Mukamel,[‡] Marco Garavelli,^{*,†} Niranjan Govind,^{*,||,⊥} and Artur Nenov^{*,†}

[†]*Dipartimento di Chimica Industriale "Toso Montanari", University of Bologna, Via Piero Gobetti 85, 40129, Bologna, Italy*

[‡]*Department of Chemistry and Department of Physics and Astronomy, University of California, Irvine, 92697, USA*

[¶]*Physics and Chemistry of Materials, Theoretical Division, Los Alamos National Laboratory, Los Alamos, NM 87545, USA*

[§]*Center for Integrated Nanotechnologies, Los Alamos National Laboratory, Los Alamos, NM 87545, USA*

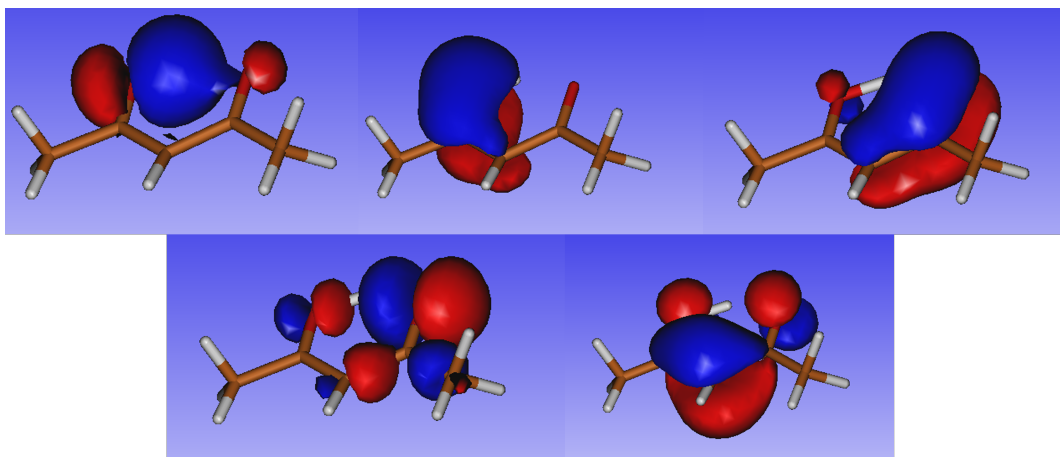
^{||}*Physical and Computational Sciences Directorate, Pacific Northwest National Laboratory, Richland, WA 99352*

[⊥]*Department of Chemistry, University of Washington, Seattle, WA 98195, USA*

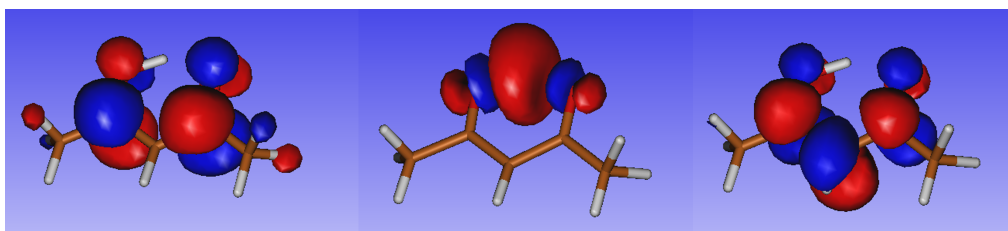
[#]*Present address: Institute of Chemistry for Life and Health Sciences (I-CLEHS) Chimie Paristech, 11 Rue Pierre et Marie Curie, 75005, Paris, France*

[@]*Present address: Materials and Process Engineering, Pratt and Whitney, Raytheon Technologies, East Hartford, CT 06118, USA*

E-mail: marco.garavelli@unibo.it; niri.govind@pnnl.gov; artur.nenov@unibo.it

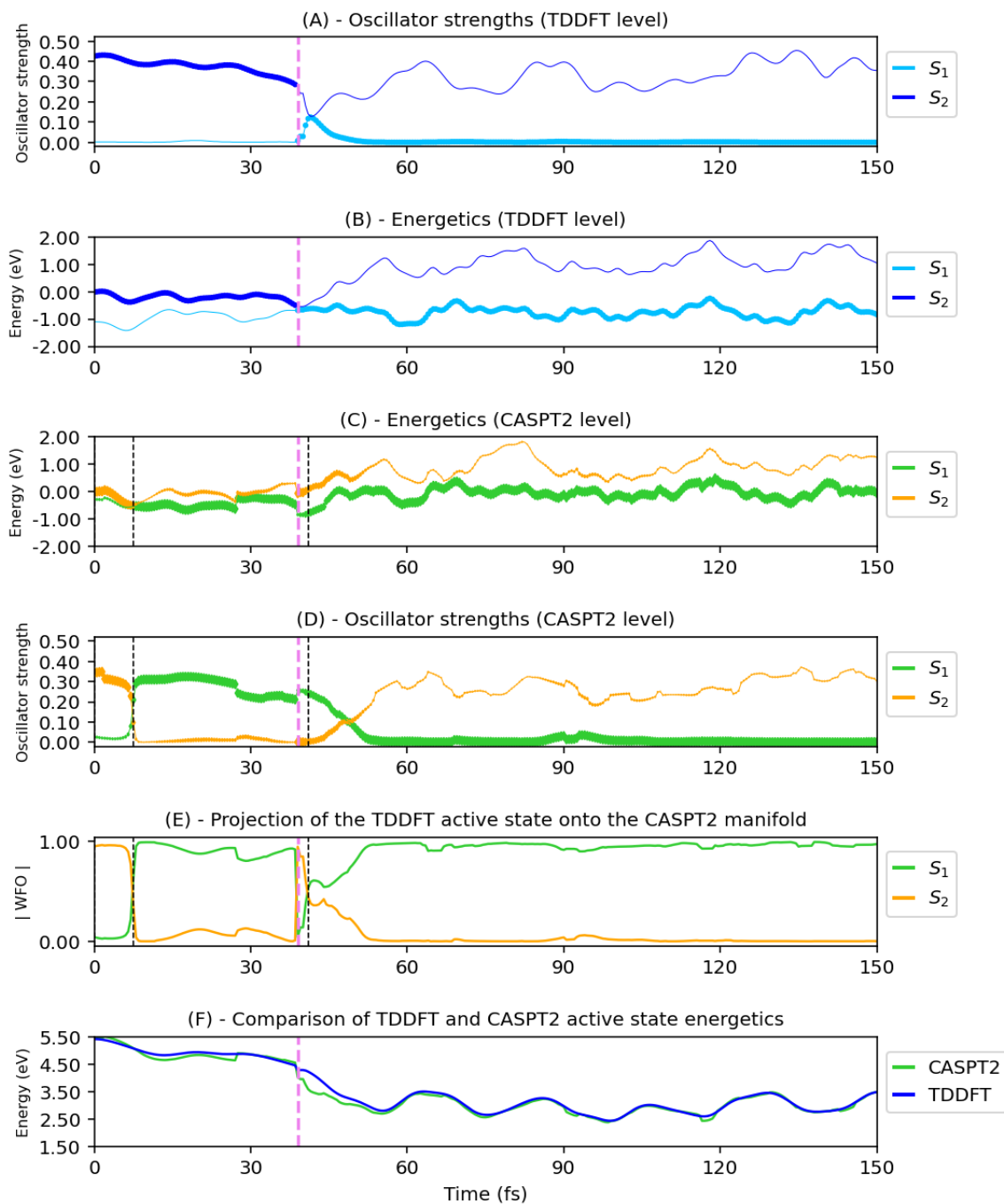


Supplementary Figure 1: Occupied molecular orbitals of the XMS-CASPT2 active space.



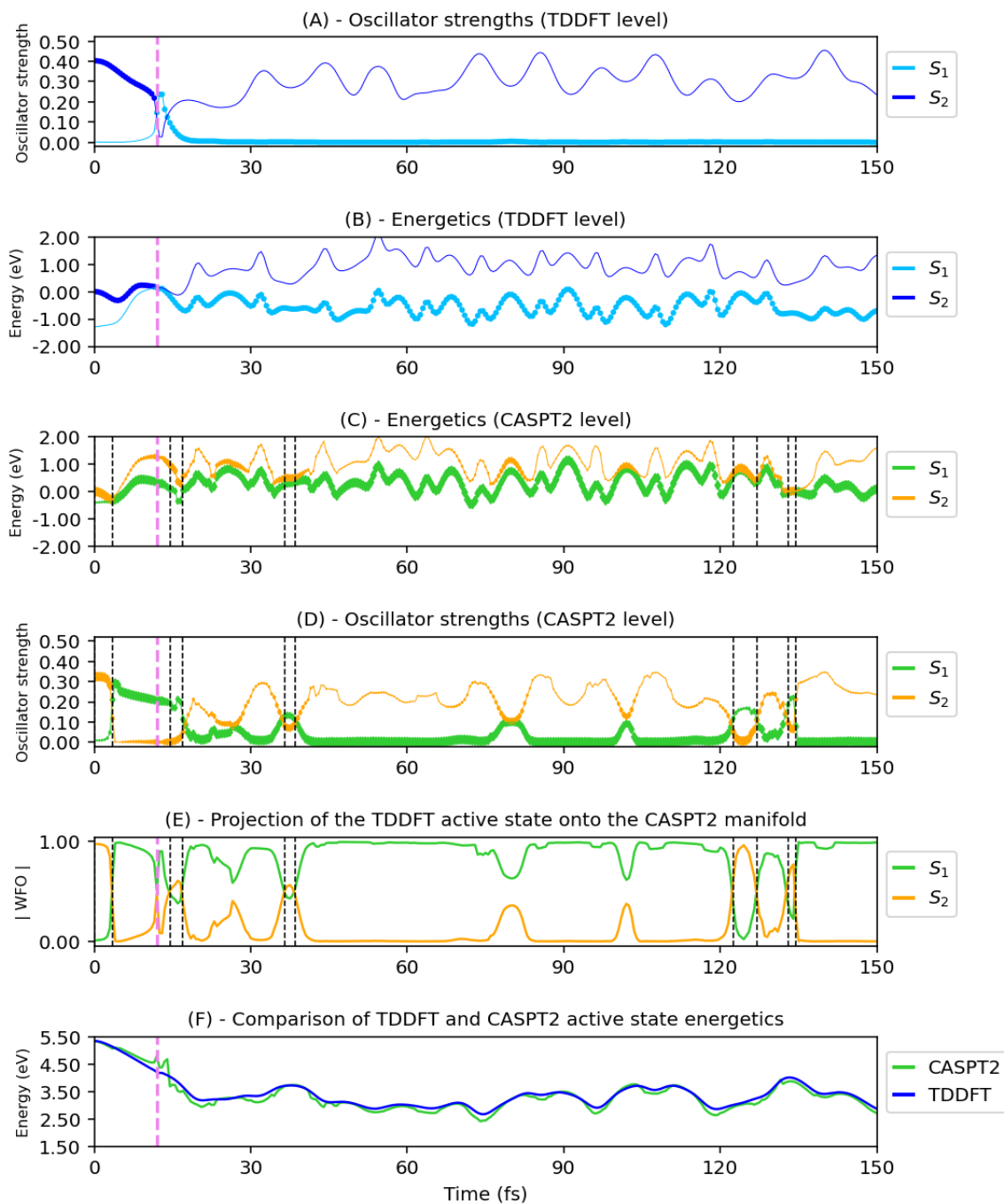
Supplementary Figure 2: Virtual molecular orbitals of the XMS-CASPT2 active space.

Sample 3



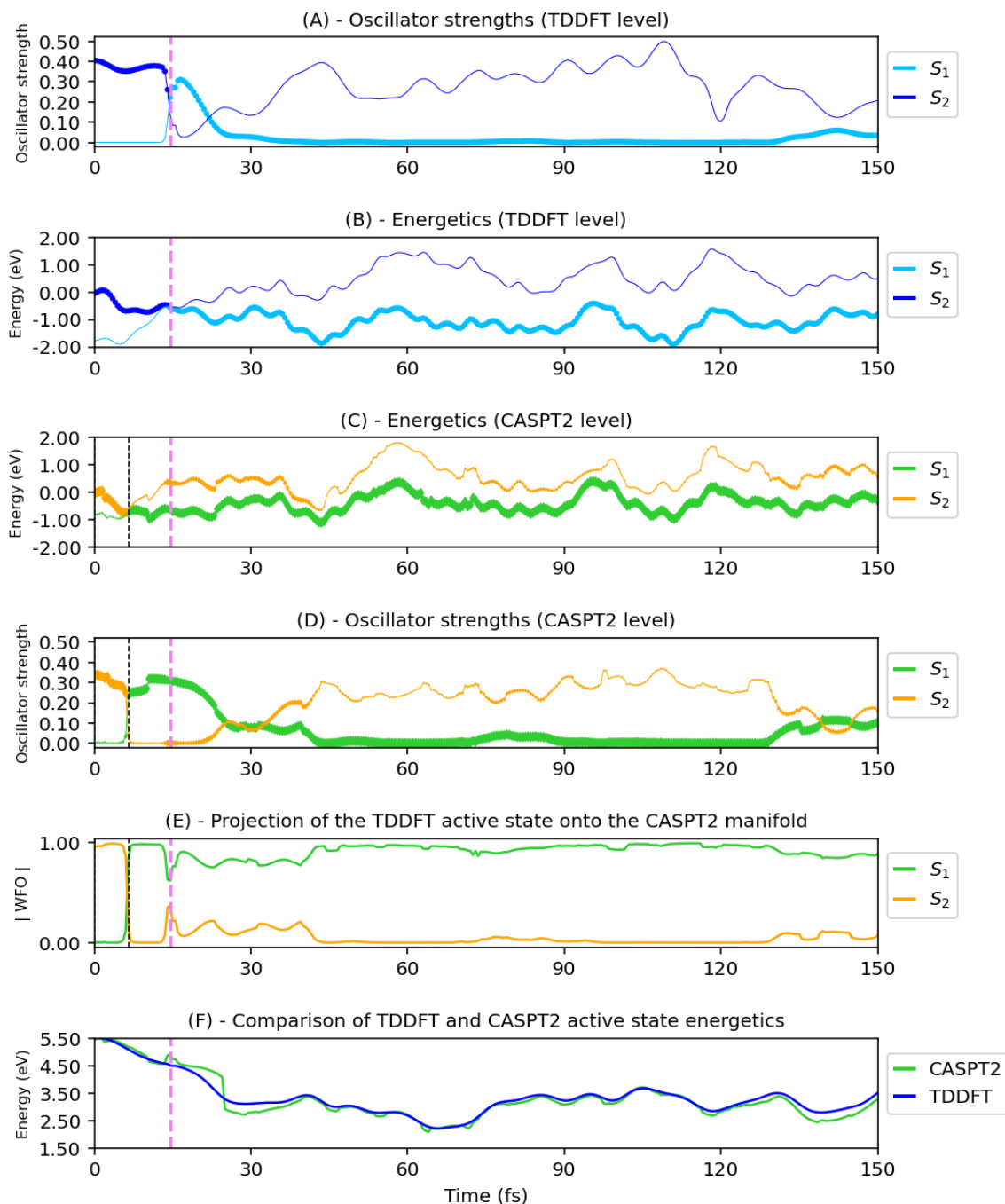
Supplementary Figure 3: Sample 3 - (A) Oscillator strengths of the two lowest excited states over the TD-DFT dynamic, highlighting the active one. (B) Energy of the three lowest excited states over the TD-DFT dynamic, highlighting the active one. (C) Energy of the two lowest excited states at CASPT2 level along the TD-DFT dynamic, highlighting the one with the highest overlap to the TD-DFT active state. (D) Oscillator strengths of the two lowest excited states at CASPT2 level over the TD-DFT dynamic, highlighting the one with the highest overlap to the TD-DFT active state; (E) Absolute value of the wavefunction overlap of the first two CASPT2 excited states with the TD-DFT active state. (F) Energy difference between active and ground state, computed at each level of theory. A fixed shift has been applied to account for the TDDFT overestimation of the $\pi\pi^*$ state energy. The line thickness in (C) and (D) is proportional to the projection of the TDDFT active state onto the CASPT2 manifold (E).

Sample 4



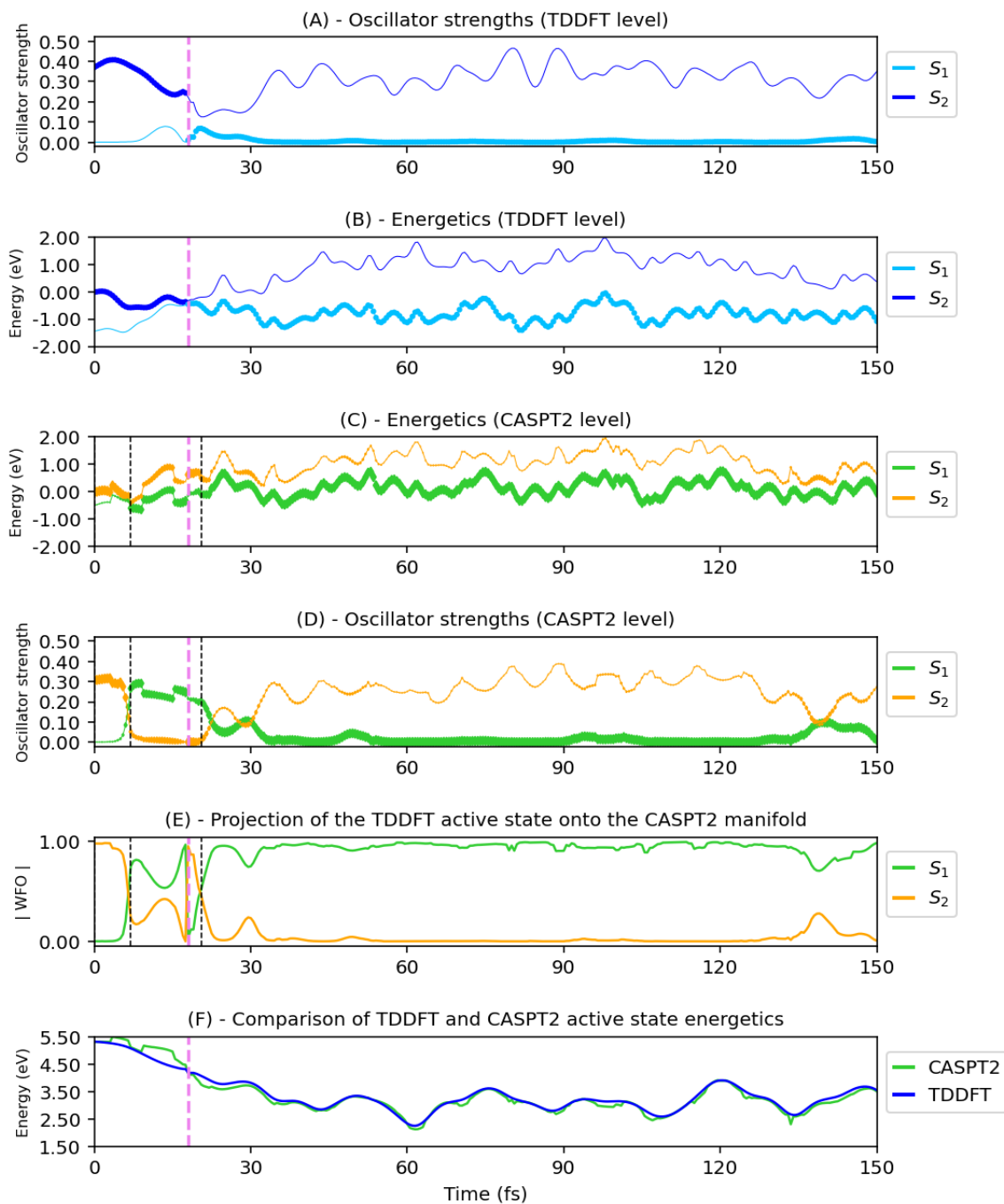
Supplementary Figure 4: Sample 4 - (A) Oscillator strengths of the two lowest excited states over the TD-DFT dynamic, highlighting the active one. (B) Energy of the three lowest excited states over the TD-DFT dynamic, highlighting the active one. (C) Energy of the two lowest excited states at CASPT2 level along the TD-DFT dynamic, highlighting the one with the highest overlap to the TD-DFT active state. (D) Oscillator strengths of the two lowest excited states at CASPT2 level over the TD-DFT dynamic, highlighting the one with the highest overlap to the TD-DFT active state; (E) Absolute value of the wavefunction overlap of the first two CASPT2 excited states with the TD-DFT active state. (F) Energy difference between active and ground state, computed at each level of theory. A fixed shift has been applied to account for the TDDFT overestimation of the $\pi\pi^*$ state energy. The line thickness in (C) and (D) is proportional to the projection of the TDDFT active state onto the CASPT2 manifold (E).

Sample 5



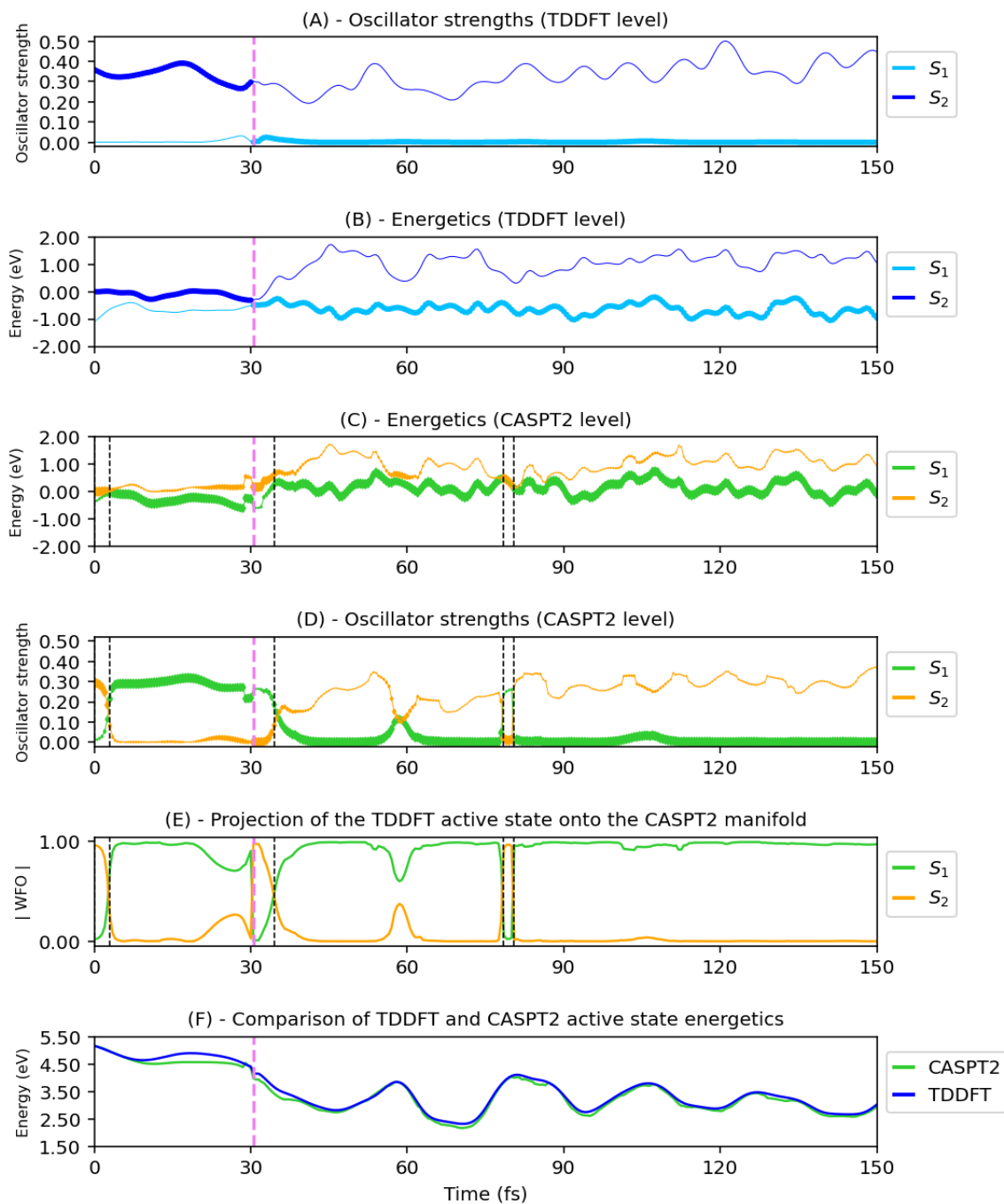
Supplementary Figure 5: Sample 5 - (A) Oscillator strengths of the two lowest excited states over the TD-DFT dynamic, highlighting the active one. (B) Energy of the three lowest excited states over the TD-DFT dynamic, highlighting the active one. (C) Energy of the two lowest excited states at CASPT2 level along the TD-DFT dynamic, highlighting the one with the highest overlap to the TD-DFT active state; (D) Oscillator strengths of the two lowest excited states at CASPT2 level over the TD-DFT dynamic, highlighting the one with the highest overlap to the TD-DFT active state. (E) Absolute value of the wavefunction overlap of the first two CASPT2 excited states with the TD-DFT active state. (F) Energy difference between active and ground state, computed at each level of theory. A fixed shift has been applied to account for the TDDFT overestimation of the $\pi\pi^*$ state energy. The line thickness in (C) and (D) is proportional to the projection of the TDDFT active state onto the CASPT2 manifold (E).

Sample 6



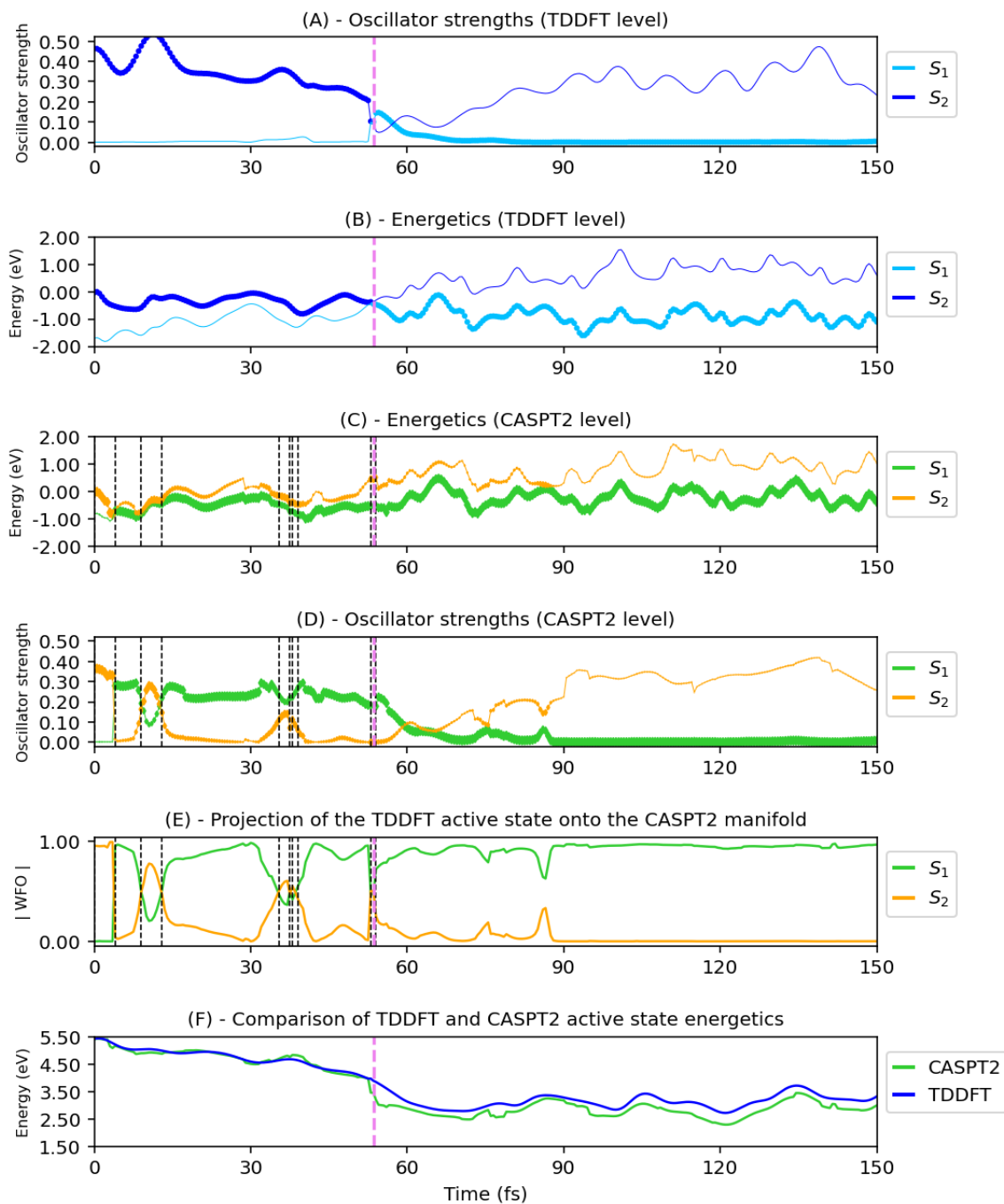
Supplementary Figure 6: Sample 6 - (A) Oscillator strengths of the two lowest excited states over the TD-DFT dynamic, highlighting the active one. (B) Energy of the three lowest excited states over the TD-DFT dynamic, highlighting the active one. (C) Energy of the two lowest excited states at CASPT2 level along the TD-DFT dynamic, highlighting the one with the highest overlap to the TD-DFT active state; (D) Oscillator strengths of the two lowest excited states at CASPT2 level over the TD-DFT dynamic, highlighting the one with the highest overlap to the TD-DFT active state. (E) Absolute value of the wavefunction overlap of the first two CASPT2 excited states with the TD-DFT active state. (F) Energy difference between active and ground state, computed at each level of theory. A fixed shift has been applied to account for the TDDFT overestimation of the $\pi\pi^*$ state energy. The line thickness in (C) and (D) is proportional to the projection of the TDDFT active state onto the CASPT2 manifold (E).

Sample 7



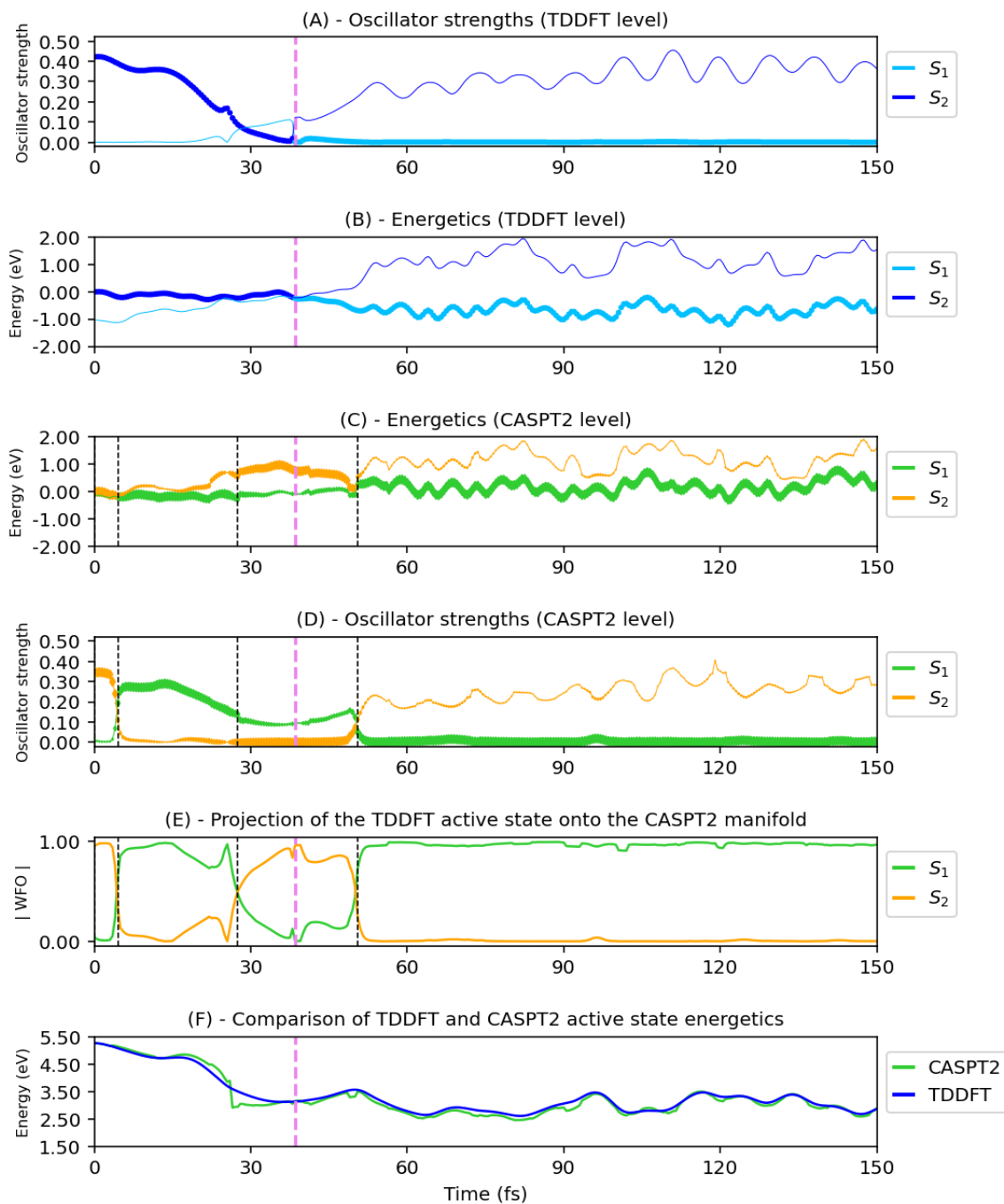
Supplementary Figure 7: Sample 7 - (A) Oscillator strengths of the two lowest excited states over the TD-DFT dynamic, highlighting the active one. (B) Energy of the three lowest excited states over the TD-DFT dynamic, highlighting the active one. (C) Energy of the two lowest excited states at CASPT2 level along the TD-DFT dynamic, highlighting the one with the highest overlap to the TD-DFT active state. (D) Oscillator strengths of the two lowest excited states at CASPT2 level over the TD-DFT dynamic, highlighting the one with the highest overlap to the TD-DFT active state; (E) Absolute value of the wavefunction overlap of the first two CASPT2 excited states with the TD-DFT active state. (F) Energy difference between active and ground state, computed at each level of theory. A fixed shift has been applied to account for the TDDFT overestimation of the $\pi\pi^*$ state energy. The line thickness in (C) and (D) is proportional to the projection of the TDDFT active state onto the CASPT2 manifold (E).

Sample 8



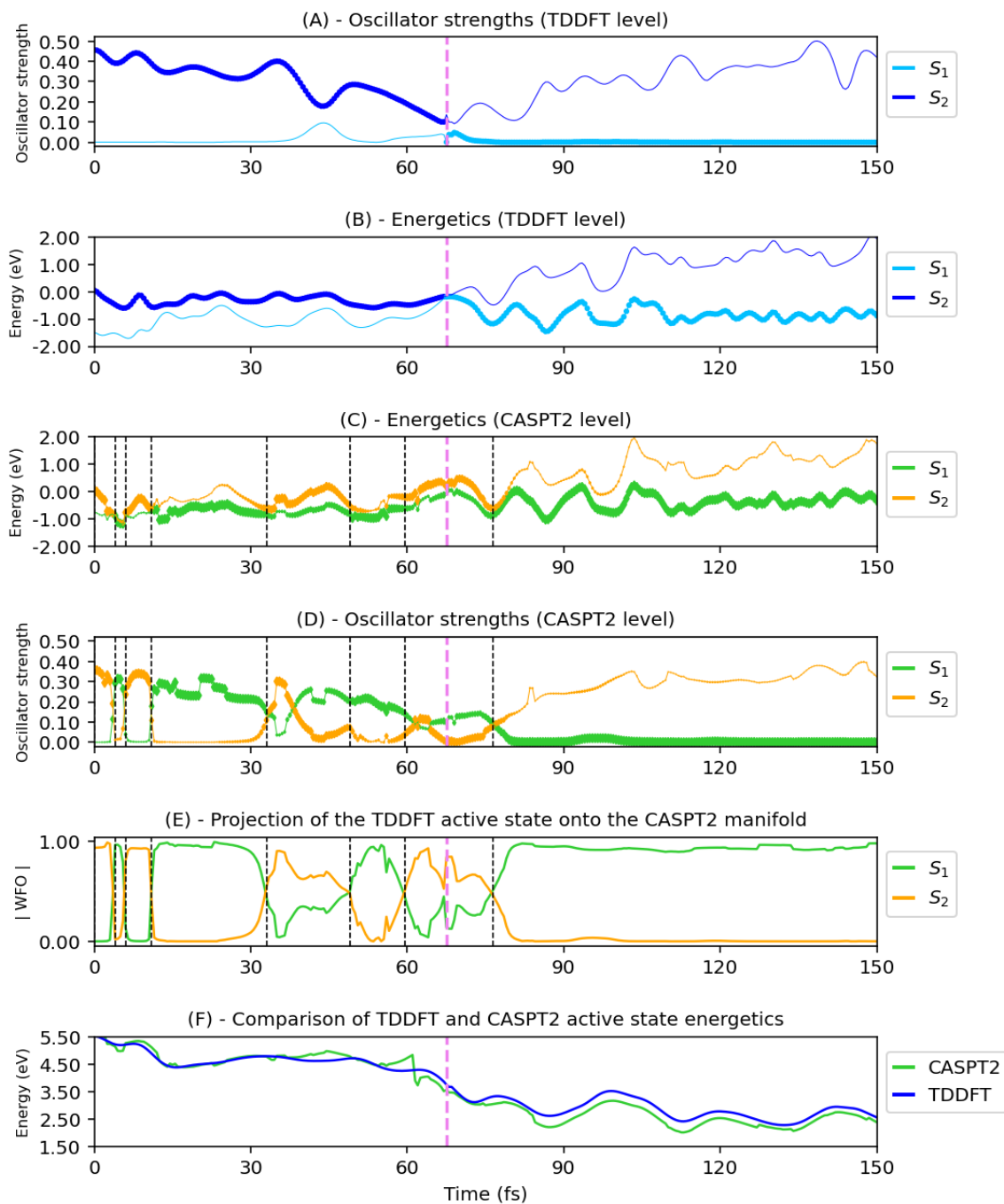
Supplementary Figure 8: Sample 8 - (A) Oscillator strengths of the two lowest excited states over the TD-DFT dynamic, highlighting the active one. (B) Energy of the three lowest excited states over the TD-DFT dynamic, highlighting the active one. (C) Energy of the two lowest excited states at CASPT2 level along the TD-DFT dynamic, highlighting the one with the highest overlap to the TD-DFT active state; (D) Oscillator strengths of the two lowest excited states at CASPT2 level over the TD-DFT dynamic, highlighting the one with the highest overlap to the TD-DFT active state. (E) Absolute value of the wavefunction overlap of the first two CASPT2 excited states with the TD-DFT active state. (F) Energy difference between active and ground state, computed at each level of theory. A fixed shift has been applied to account for the TDDFT overestimation of the $\pi\pi^*$ state energy. The line thickness in (C) and (D) is proportional to the projection of the TDDFT active state onto the CASPT2 manifold (E).

Sample 9



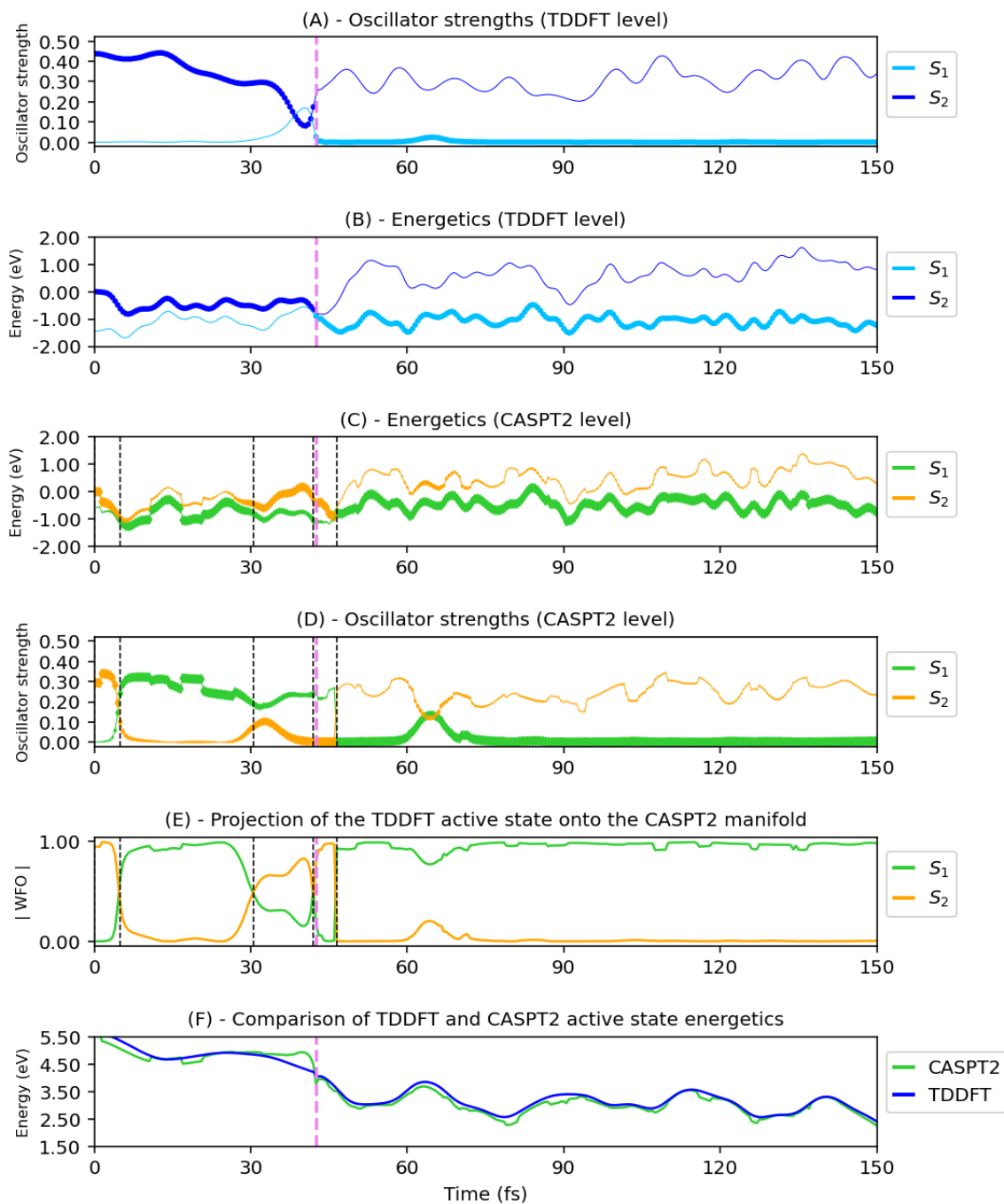
Supplementary Figure 9: Sample 9 - (A) Oscillator strengths of the two lowest excited states over the TD-DFT dynamic, highlighting the active one. (B) Energy of the three lowest excited states over the TD-DFT dynamic, highlighting the active one. (C) Energy of the two lowest excited states at CASPT2 level along the TD-DFT dynamic, highlighting the one with the highest overlap to the TD-DFT active state; (D) Oscillator strengths of the two lowest excited states at CASPT2 level over the TD-DFT dynamic, highlighting the one with the highest overlap to the TD-DFT active state. (E) Absolute value of the wavefunction overlap of the first two CASPT2 excited states with the TD-DFT active state. (F) Energy difference between active and ground state, computed at each level of theory. A fixed shift has been applied to account for the TDDFT overestimation of the $\pi\pi^*$ state energy. The line thickness in (C) and (D) is proportional to the projection of the TDDFT active state onto the CASPT2 manifold (E).

Sample 10



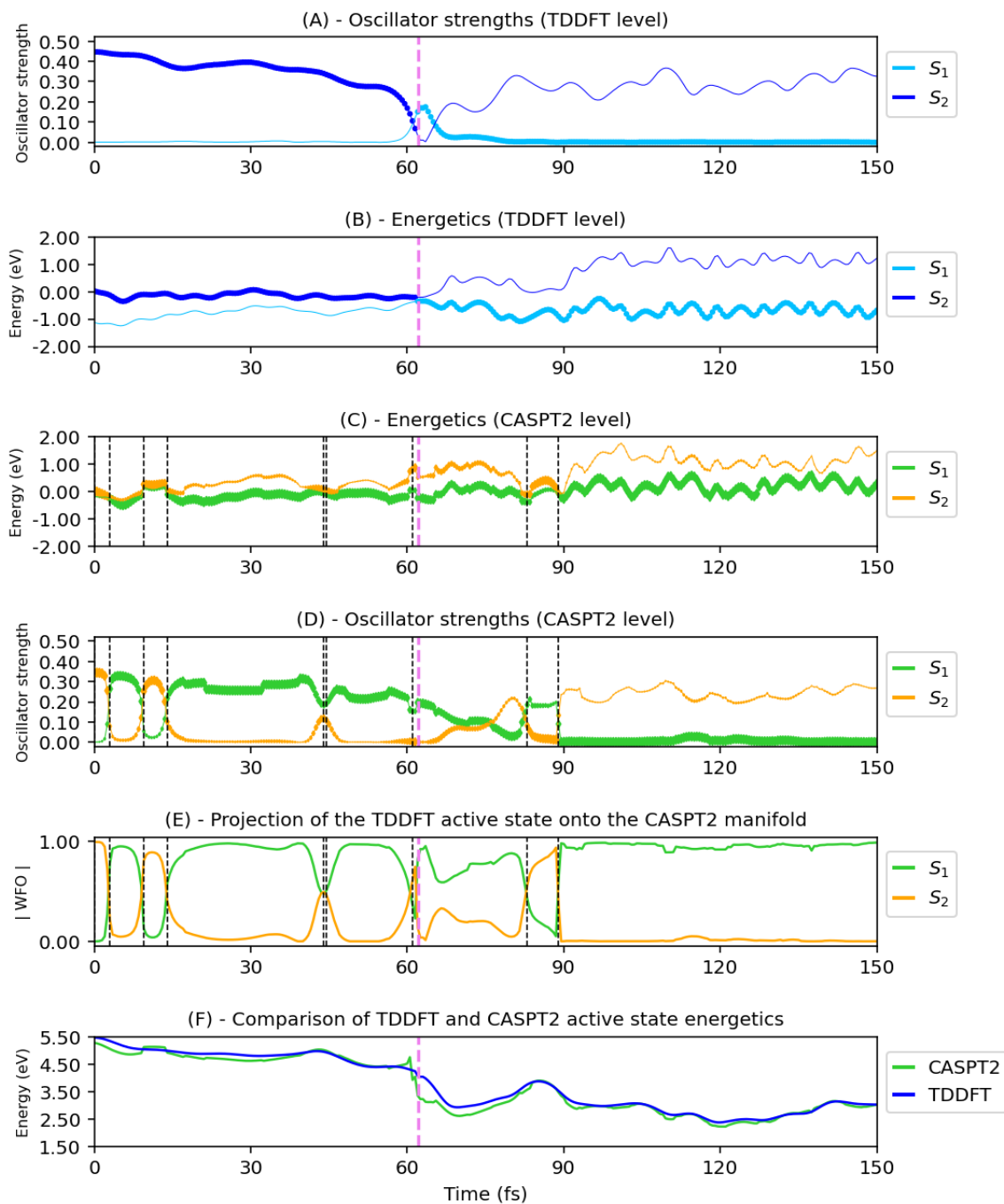
Supplementary Figure 10: Sample 10 - (A) Oscillator strengths of the two lowest excited states over the TD-DFT dynamic, highlighting the active one. (B) Energy of the three lowest excited states over the TD-DFT dynamic, highlighting the active one. (C) Energy of the two lowest excited states at CASPT2 level along the TD-DFT dynamic, highlighting the one with the highest overlap to the TD-DFT active state; (D) Oscillator strengths of the two lowest excited states at CASPT2 level over the TD-DFT dynamic, highlighting the one with the highest overlap to the TD-DFT active state. (E) Absolute value of the wavefunction overlap of the first two CASPT2 excited states with the TD-DFT active state. (F) Energy difference between active and ground state, computed at each level of theory. A fixed shift has been applied to account for the TDDFT overestimation of the $\pi\pi^*$ state energy. The line thickness in (C) and (D) is proportional to the projection of the TDDFT active state onto the CASPT2 manifold (E).

Sample 11

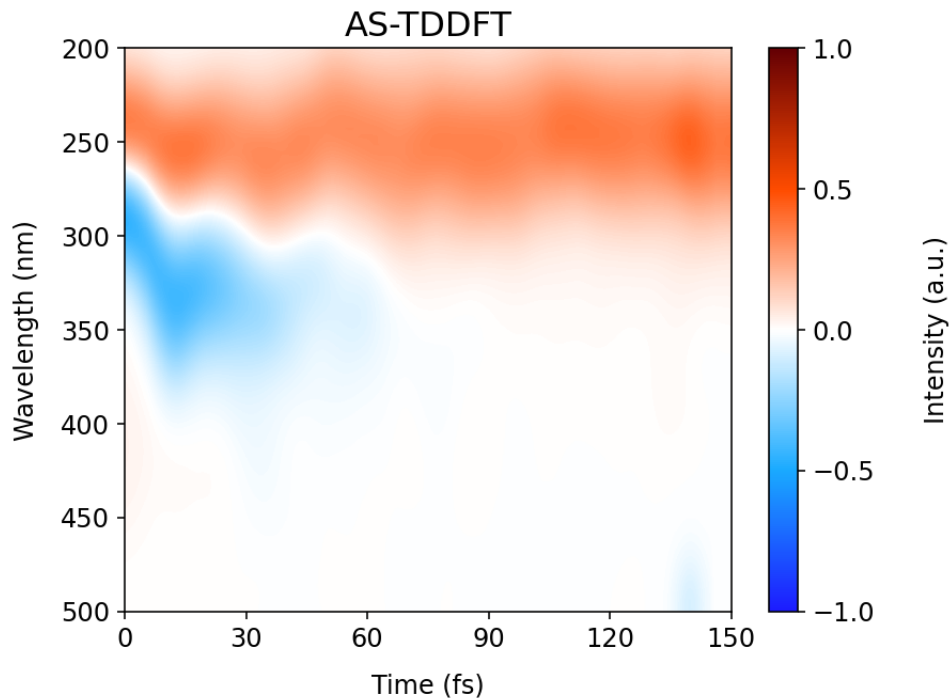


Supplementary Figure 11: Sample 11 - (A) Oscillator strengths of the two lowest excited states over the TD-DFT dynamic, highlighting the active one. (B) Energy of the three lowest excited states over the TD-DFT dynamic, highlighting the active one. (C) Energy of the two lowest excited states at CASPT2 level along the TD-DFT dynamic, highlighting the one with the highest overlap to the TD-DFT active state; (D) Oscillator strengths of the two lowest excited states at CASPT2 level over the TD-DFT dynamic, highlighting the one with the highest overlap to the TD-DFT active state. (E) Absolute value of the wavefunction overlap of the first two CASPT2 excited states with the TD-DFT active state. (F) Energy difference between active and ground state, computed at each level of theory. A fixed shift has been applied to account for the TDDFT overestimation of the $\pi\pi^*$ state energy. The line thickness in (C) and (D) is proportional to the projection of the TDDFT active state onto the CASPT2 manifold (E).

Sample 12



Supplementary Figure 12: Sample 12 - (A) Oscillator strengths of the two lowest excited states over the TD-DFT dynamic, highlighting the active one. (B) Energy of the three lowest excited states over the TD-DFT dynamic, highlighting the active one. (C) Energy of the two lowest excited states at CASPT2 level along the TD-DFT dynamic, highlighting the one with the highest overlap to the TD-DFT active state; (D) Oscillator strengths of the two lowest excited states at CASPT2 level over the TD-DFT dynamic, highlighting the one with the highest overlap to the TD-DFT active state. (E) Absolute value of the wavefunction overlap of the first two CASPT2 excited states with the TD-DFT active state. (F) Energy difference between active and ground state, computed at each level of theory. A fixed shift has been applied to account for the TDDFT overestimation of the $\pi\pi^*$ state energy. The line thickness in (C) and (D) is proportional to the projection of the TDDFT active state onto the CASPT2 manifold (E).



Supplementary Figure 13: Simulated transient absorption spectrum of AcAc obtained through averaging of 50 excited state trajectories. The signal at higher energy (dark-orange) is assigned to excited state absorption (ESA), while the one at lower energy (blue) is assigned to stimulated emission (SE) from the active state to the ground state. Ground state bleaching (GSB) is not included.

Supplementary Table 1: Energies of the first two excited states alongside their energy difference, computed at the Franck-Condon point for different TDDFT functionals and for CASPT2, where the latter is used as a reference for evaluating the functionals' correctness.

Level of theory	$E(S_1)$ (eV)	$E(S_2)$ (eV)	$\Delta E (S_2-S_1)$ (eV)
CAM-B3LYP	4.515	5.597	1.082
PBE0	4.385	5.563	1.178
LC-wHPBE	4.618	5.652	1.035
M06	4.342	5.573	1.230
XMS-24-CASPT2(10,8)	4.223	4.517	0.294